Neuron

Article

Feature-tuned synaptic inputs to somatostatin interneurons drive context-dependent processing

Graphical abstract

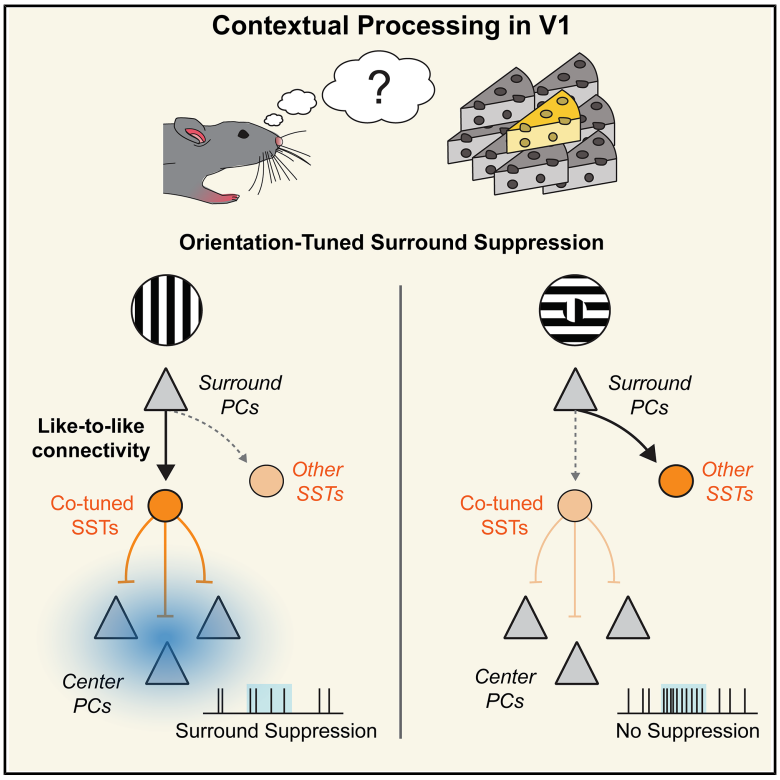

Highlights

- Tuned excitation in SSTs explains their figure/ground modulation
- Pyramidal cells (PCs) provide tuned excitation to SSTs from the surround
- Single-cell optogenetics reveals a like-to-like PC→SST connectivity motif
- This precise circuit architecture implements contextual modulation

Authors

William D. Hendricks, Masato Sadahiro, Dan Mossing, Julia Veit, Hillel Adesnik

Correspondence

hadesnik@berkeley.edu

In brief

Combining intracellular and extracellular recordings, calcium imaging, and holographic circuit mapping, Hendricks et al. identify a feature-specific pyramidal cell-to-somatostatin interneuron microcircuit in the visual cortex. This tuned "like-to-like" pattern of excitatory synaptic architecture implements contextual computations that may underlie figure/ground perception.

Hendricks et al., 2026, Neuron *114*, 1–12
April 1, 2026
https://doi.org/10.1016/j.neuron.2025.12.021

CellPress

Neuron

CellPress
OPEN ACCESS

Article

Feature-tuned synaptic inputs to somatostatin interneurons drive context-dependent processing

William D. Hendricks,[1,5] Masato Sadahiro,[1,5] Dan Mossing,[1,2] Julia Veit,[3] and Hillel Adesnik[1,4,6,*]
[1]Department of Neuroscience, University of California, Berkeley, Berkeley, CA, USA
[2]Biophysics Graduate Group, University of California, Berkeley, Berkeley, CA, USA
[3]Department of Physiology, University of Freiburg, Freiburg, Germany
[4]The Helen Wills Neuroscience Institute, University of California, Berkeley, Berkeley, CA, USA
[5]These authors contributed equally
[6]Lead contact
*Correspondence: hadesnik@berkeley.edu
https://doi.org/10.1016/j.neuron.2025.12.021

SUMMARY

Mapping neural computation onto the functional microarchitecture of sensory circuits is essential for understanding how brain circuits transform input signals into coherent percepts. Many higher-order perceptual processes emerge in the cortex, yet relatively little is known about how specific connectivity motifs give rise to these computations. To address this challenge, we combined single-cell and population-level physiological recordings and perturbation methods to map a context-dependent cortical computation onto the synaptic microarchitecture of the mouse primary visual cortex (V1). We demonstrate a precise pattern of synaptic connectivity from cortical pyramidal cells (PCs) to somatostatin (SST) inhibitory interneurons that mediates context-driven figure/ground modulation in V1. Through a like-to-like connectivity rule from PCs to SSTs, this circuit explains SSTs' visual encoding properties and their resulting impact on contextual modulation in V1. These findings reveal key synaptic and circuit mechanisms that may underlie the earliest stages of scene segmentation in the visual cortex.

INTRODUCTION

Connectivity patterns between cortical neurons are the building blocks of cortical computations. Yet, mapping specific computations onto the synaptic and circuit architecture of cortical circuits has proved challenging. Powerful approaches that correlate physiological response properties of cortical neurons with their connectivity patterns have revealed feature-specific wiring among nearby excitatory neurons,[1–10] providing a circuit basis for the amplification of correlated neural activity. However, these findings have yet to explain higher-level computations that may rely on specific connectivity patterns between excitatory neurons and local inhibitory interneurons.[9,11–15] Moreover, precise perturbations of neural activity are necessary to determine which connectivity features causally drive distinct aspects of cortical computation.

One of the first computations the visual system must perform is segregating figures from the background. A neural correlate of figure segmentation appears as early as the primary visual cortex (V1): the response of V1 neurons is much greater to a stimulus within their receptive fields when it constitutes a "figure" than when that same stimulus forms part of the background, a phenomenon known as "figure/ground modulation."[11,16–19] Physiologically, a clear neural correlate of this modulation manifests as "orientation-dependent surround suppression."[17,20–25] In primates, cats, and mice, studies show that the relative orientation of the center and surround of a visual grating profoundly modulates V1 neural responses.[11,12,16,17,20–22,24–27] When the center orientation differs from the surround ("cross-oriented"), leading to the percept of a figure, V1 neurons are potently driven.[20–24] Conversely, when the center orientation matches that of the surround ("iso-oriented"), removing the percept of a figure, V1 neurons are strongly suppressed.[25–28] Thus, orientation-dependent surround suppression is a widely conserved feature of visual cortical activity that may represent one of the earliest cortical computations supporting the segmentation of the visual scene.[16,19,21,23,24,29]

Surround suppression in L2/3 depends on the activity of somatostatin-positive GABAergic interneurons (SSTs).[14,15] When a grating extends beyond the classical receptive field (CRF) of L2/3 pyramidal cells (PCs), SSTs are potently recruited[12,14,30,31] and inhibit both PCs and parvalbumin (PV)-positive interneurons (PVs).[32–36] The net inhibition of the PC/PV network suppresses total synaptic activity,[37–39] which results in greatly reduced spiking for both PCs and PVs. However, when the grating covering the surround does not match that of the center, the spiking activity of PCs and PVs is not suppressed and can even be facilitated.[11,12,20,39] This orientation-dependent

Please cite this article in press as: Hendricks et al., Feature-tuned synaptic inputs to somatostatin interneurons drive context-dependent processing, Neuron (2025), https://doi.org/10.1016/j.neuron.2025.12.021

component of surround suppression still lacks a complete synaptic and circuit mechanistic understanding. More generally, we lack a circuit-level understanding that explains how figure/ground modulation emerges from the functional microarchitecture of V1 between PCs, SSTs, and other cell types.

Recent studies[11,12] have shown that non-matching surrounds drive vasoactive-intestinal peptide (VIP) neurons, which selectively inhibit SSTs,[33,35,40–42] potentially supporting a model where VIP→SST inhibition is the key means for generating figure/ground modulation. However, optogenetic silencing of VIPs only partially reduces the orientation dependence of surround suppression.[11,12] Thus, whether the inhibitory action of VIPs onto SSTs is essential to tuning the orientation dependence of surround suppression or whether they play a more modulatory role remains uncertain. An alternative—or perhaps even complementary—possibility is that SSTs are selectively driven by matching surrounds because only matching surrounds drive sufficiently strong afferent synaptic excitation. This latter model focuses on the excitatory input patterns to SSTs and would likely require a high degree of specificity in their synaptic input architecture: SSTs would have to receive excitation preferentially from pools of PCs with the same orientation preference. Indeed, SSTs are sharply orientation tuned to full-field gratings, similar to PCs, suggesting that they receive strong, tuned excitatory input.[43] However, there is still no direct evidence for such a high degree of specificity of excitatory input to SSTs or to cortical GABAergic neurons in general.

To determine the neural mechanisms of figure/ground modulation, we combined extracellular electrophysiology, two-photon (2p) calcium imaging, *in vivo* whole-cell recording, and one-photon and 2p optogenetics to map a context-dependent computation onto the synaptic and circuit architecture of the mouse V1. We reveal a previously unknown level of specificity in the excitatory input connectivity from L2/3 PCs to SSTs and demonstrate how this circuitry, combined with other recurrent circuits in V1, implements this fundamental visual computation. These findings illuminate a synaptic mechanism for the encoding of contextual information and suggest that such feature-dependent connectivity from PC→SSTs may represent a general principle by which cortical circuits support higher-level computations.

RESULTS

Synaptic basis of figure/ground modulation in V1

First, we probed figure/ground modulation in V1 using extracellular electrophysiology. When the orientation of the surround matched that of the center (“iso”), V1 neuron activity was strongly suppressed (Figures 1A–1C). In contrast, when the orientation of the surround was orthogonal to that of the center (“cross”), this suppression largely disappeared. Although this phenomenon is well documented at the spike-rate level, its synaptic basis remains poorly understood. Prior work has shown that iso-oriented surrounds drive suppression by decreasing total synaptic input (i.e., reducing both synaptic excitation and inhibition) and by lowering the ratio between visually evoked excitation and inhibition.[37] Cross-oriented surrounds might counteract this suppression by selectively increasing excitatory input, by reducing inhibitory input, or by preventing the surround-induced suppression of total synaptic input. To directly distinguish between these possibilities, we made *in vivo* whole-cell recordings from layer 2/3 PCs in awake mice, enabling direct measurement of excitatory and inhibitory postsynaptic currents (EPSCs and IPSCs, respectively) underlying surround suppression. Center gratings at the neuron’s preferred orientation evoked strong EPSCs and IPSCs in PCs, while the addition of the iso-oriented surround substantially suppressed both synaptic excitation and inhibition, indicative of network suppression (Figures 1D and 1E). This is consistent with prior work in mouse V1, which showed that, although synaptic inhibition increases over a broader range of stimulus sizes compared with excitation, both show a net decrease for the largest sizes.[37] Conversely, addition of a cross-oriented surround restored excitation and inhibition to values indistinguishable from those of the center alone. The results of these intracellular recordings show that cross-oriented gratings avoid driving surround suppression by preventing the network suppression of total synaptic input. Exactly how this occurs, however, requires further investigation into the cell types and cell-type-specific connectivity in V1.

Cortical SST neurons are critical for figure/ground modulation

SST activity is required for surround suppression,[14] but whether SSTs contribute to the orientation tuning of surround suppression is unclear. Thus, we considered the V1 microcircuit and inputs to SSTs (Figure 2A) and employed somatic 2p calcium imaging in transgenic mice (see STAR Methods). First, we confirmed that PCs preferred cross-oriented gratings (Figure 2B), similar to the preferences seen in our extracellular and intracellular recordings (Figure 1). Notably, however, SSTs strongly preferred iso-oriented compared with cross-oriented gratings (Figure 2C), which was strikingly opposite to the preferences of PCs (Figure 2B) as well as PVs (Figure S1).

To determine whether SST activity is a necessary component of orientation-dependent surround suppression, we used multielectrode arrays to record activity from regular-spiking (RS) putative excitatory neurons and fast-spiking (FS) putative PV interneurons while optogenetically silencing SSTs using eNpHR3.0 (see STAR Methods). If their activity is critical, then silencing SSTs should attenuate orientation-dependent surround suppression. We computed the “contextual modulation index” (CMI) to use as a direct measure of figure/ground modulation. CMI compares the amount of surround suppression between the iso and cross conditions ($CMI = (R_{cross} - R_{iso}) / (R_{cross} + R_{iso})$, where R is the mean visual response averaged across all orientations). Thus, a CMI of −1 represents a complete preference for iso gratings, 0 indicates no preference, and 1 represents a complete preference for cross gratings. CMI was broadly distributed and almost always positive (Figure S1), reflective of robust orientation-dependent surround suppression. We found no difference in CMI between FS and RS units (Figure S1) or between running and stationary states (Figure S2), even though we did confirm a reduction in the surround suppression index. Silencing SSTs increased both RS and FS unit activity (Figure S2). Strikingly, silencing SSTs significantly decreased CMI, demonstrating that SST activity critically contributes to the orientation dependence of surround suppression in V1 (Figure 2D). Notably, because

Please cite this article in press as: Hendricks et al., Feature-tuned synaptic inputs to somatostatin interneurons drive context-dependent processing, Neuron (2025), https://doi.org/10.1016/j.neuron.2025.12.021

CellPress
OPEN ACCESS

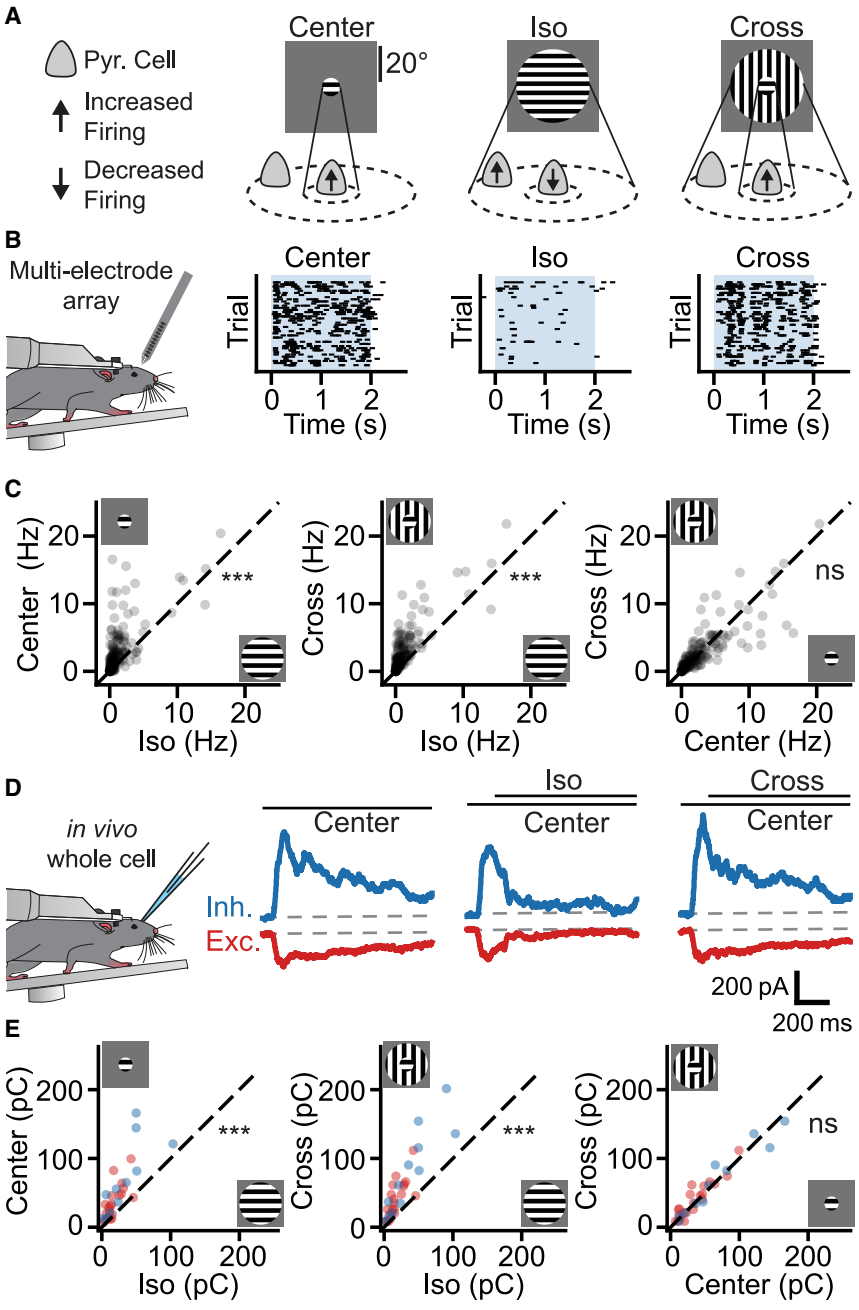

Figure 1. Synaptic mechanism of orientation-dependent surround suppression in the primary visual cortex

(A) Figure/ground segregation in mouse primary visual cortex (V1) exemplified as orientation-dependent surround suppression. A "center" or "figure" visual stimulus (left) potently drives neural activity in a pyramidal cell (PC), whereas the same stimulus extending into the surround ("iso," middle) suppresses it. When the surround does not match the center ("cross," right), neural activity is no longer suppressed.

(B) Extracellular recordings in mouse V1 (schematic, left) in response to center, iso, and cross gratings. Raster plots (right 3 panels) are taken from an example regular-spiking (RS) unit. Shaded blue region marks the timing of the visual stimulus.

(C) Scatterplots comparing RS unit responses (n = 160 units) to center vs. iso (left, $p < 10^{-5}$), iso vs. cross (middle, $p < 10^{-5}$), and cross vs. center (right, $p = 0.676$) gratings. p values were calculated using Wilcoxon signed-rank test and corrected for multiple comparisons using Holm's method.

(D) Whole-cell voltage-clamp recordings from putative PCs in V1 (schematic, left) taken from awake, head-fixed animals. Excitatory (red, n = 21 cells) and inhibitory (blue, n = 12 cells) current responses to center only, center with iso, and center with cross grating. Note that in these experiments, the surround stimulus switched on ~150 ms after the center. Dashed line represents the baseline holding current for excitatory (−70 mV) and inhibitory (0 mV) potentials. The traces represent the grand average visual responses across cells. Solid black lines above the traces represent timing of the visual stimuli.

(E) Scatterplots comparing synaptic charge transfer (in pC) of EPSCs (red, n = 21 cells) and IPSCs (blue, n = 12 cells) to center vs. iso (left, $p < 10^{-4}$), iso vs. cross (middle, $p < 10^{-5}$), and cross vs. center (right, $p = 0.111$) gratings. p values were calculated using Wilcoxon signed-rank test and corrected for multiple comparisons using Holm's method. ***$p < 0.001$; ns, not significant.

FS units largely correspond to PV interneurons, these results demonstrate that SST activity simultaneously modulates the visual representations in both PCs and PVs. As PVs are the primary source of somatic inhibition of PCs, this implies that the end effect of SSTs on the network is a combination of direct (putatively dendritic) inhibition of PCs and a reduction in somatic inhibition. The net effect on the population is a reduction in orientation-dependent surround suppression.

An SST switch-on model for figure/ground modulation

Based on the foregoing data, we can conceive of a model in which iso-oriented surround stimuli recruit SSTs, driving network suppression of total synaptic activity, thereby reducing network firing rates. Cross-oriented stimuli then would not recruit SSTs, avoiding this network suppression, leaving firing rates intact, and giving rise to figure/ground modulation. However, this conceptual model still requires a synaptic mechanism that explains the selective recruitment of SSTs for iso-oriented, but not cross-oriented, stimuli. We can consider two scenarios: first, VIPs, which preferentially inhibit SSTs, might specifically "switch off" SSTs for cross-oriented stimuli, thereby preventing surround suppression.[11,12] Alternatively, iso-oriented gratings, but not cross-oriented gratings, could specifically "switch on" SSTs and thereby engage surround suppression. In the first case, a

Please cite this article in press as: Hendricks et al., Feature-tuned synaptic inputs to somatostatin interneurons drive context-dependent processing, Neuron (2025), https://doi.org/10.1016/j.neuron.2025.12.021

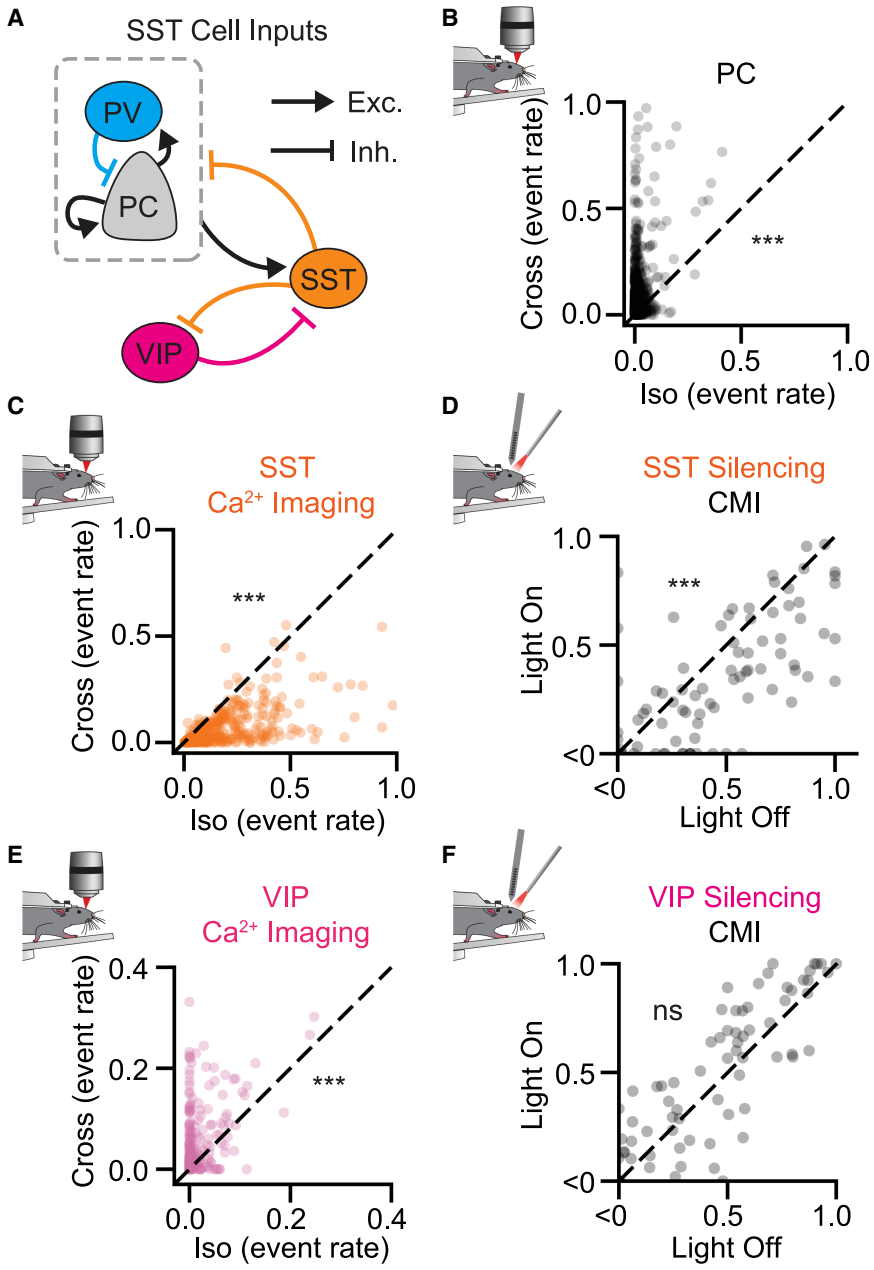

Figure 2. Somatostatin interneurons are required for orientation-dependent surround suppression

(A) Schematic of the L2/3 V1 microcircuit between PCs (gray), PVs (blue), SSTs (orange), and VIPs (pink).

(B) Scatterplots comparing PC visual responses in the iso and cross conditions. Activity is measured as the deconvolved event rate, see STAR Methods for details (n = 2,329 cells, $p < 10^{-5}$, Wilcoxon signed-rank test). Somatic calcium imaging recordings were made from CaMK2a-tTa;tetO-GCaMP6s mice.

(C) Similar to (B), except for SSTs (n = 362 cells, $p < 10^{-5}$, Wilcoxon signed-rank test). Recordings were made from SST-IRES-Cre;TITL-GCaMP6s (Ai162) mice.

(D) Scatterplot comparing contextual modulation index (CMI) in the "light-on" and "light-off" optogenetic silencing conditions of SST cells (n = 83 RS units, $p < 10^{-5}$, Wilcoxon signed-rank test). Multi-electrode array recordings were made from SST-IRES-Cre mice injected with DIO-eNpHR3.0-YFP.

(E) Similar to (C) for VIPs (n = 318 cells, $p < 10^{-5}$, Wilcoxon signed-rank test). Somatic calcium imaging recordings made from VIP-IRES-Cre × TITL-GCaMP6s (Ai162) mice.

(F) Same as in (D) for VIP silencing (n = 71 RS units, p = 0.066, Wilcoxon signed-rank test). Multi-electrode array recordings were made from VIP-IRES-Cre mice injected with DIO-eNpHR3.0-YFP. See also Figures S1–S3. ***$p < 0.001$; ns, not significant.

surround grating of any orientation is sufficient to excite SSTs, but VIP activity cancels this excitation. In the latter case, only iso-oriented gratings generate sufficient excitation in SSTs to drive firing. Moreover, both of these mechanisms could exist in tandem, operating synergistically with one another to modulate figure/ground perception.

To examine the switch-off hypothesis, we measured visual responses of VIPs to iso- and cross-oriented stimuli and probed the network impact of optogenetically silencing their activity. 2p calcium imaging from VIPs showed that nearly all VIPs responded more strongly to cross-oriented than to iso-oriented stimuli (Figure 2E), consistent with prior findings.[11,12] To test whether VIPs have a causal role in the orientation dependence of surround suppression, we optogenetically suppressed their activity and measured the impact on V1 activity and the CMI. Illumination of VIPs expressing the silencer eNpHR3.0 strongly suppressed their visually evoked activity and reduced PC activity (Figure S2), confirming the efficacy of our manipulation. Surprisingly, despite the strong effect that VIP silencing had on V1 firing rates in both the cross and iso conditions (Figure S2), our manipulation had no detectable effect on CMI (Figure 2F), implying that VIP activity is not essential for the orientation dependence of surround suppression. Given that two prior studies found that optogenetically suppressing VIPs altered this contextual modulation,[11,12] we considered the possibility that an effect on CMI was not detectable with our sample size. Thus, we executed an analogous experiment optogenetically suppressing VIPs while sampling a much larger pool of PCs with somatic 2p calcium imaging, as done in one of these prior studies.[12] In this case, we found that VIP silencing drove a statistically significant, albeit partial, effect on CMI (Figure S3), both qualitatively and quantitatively consistent with prior work.[11,12] However, the remaining contextual modulation after VIP suppression suggests that there must

Please cite this article in press as: Hendricks et al., Feature-tuned synaptic inputs to somatostatin interneurons drive context-dependent processing, Neuron (2025), https://doi.org/10.1016/j.neuron.2025.12.021

CellPress
OPEN ACCESS

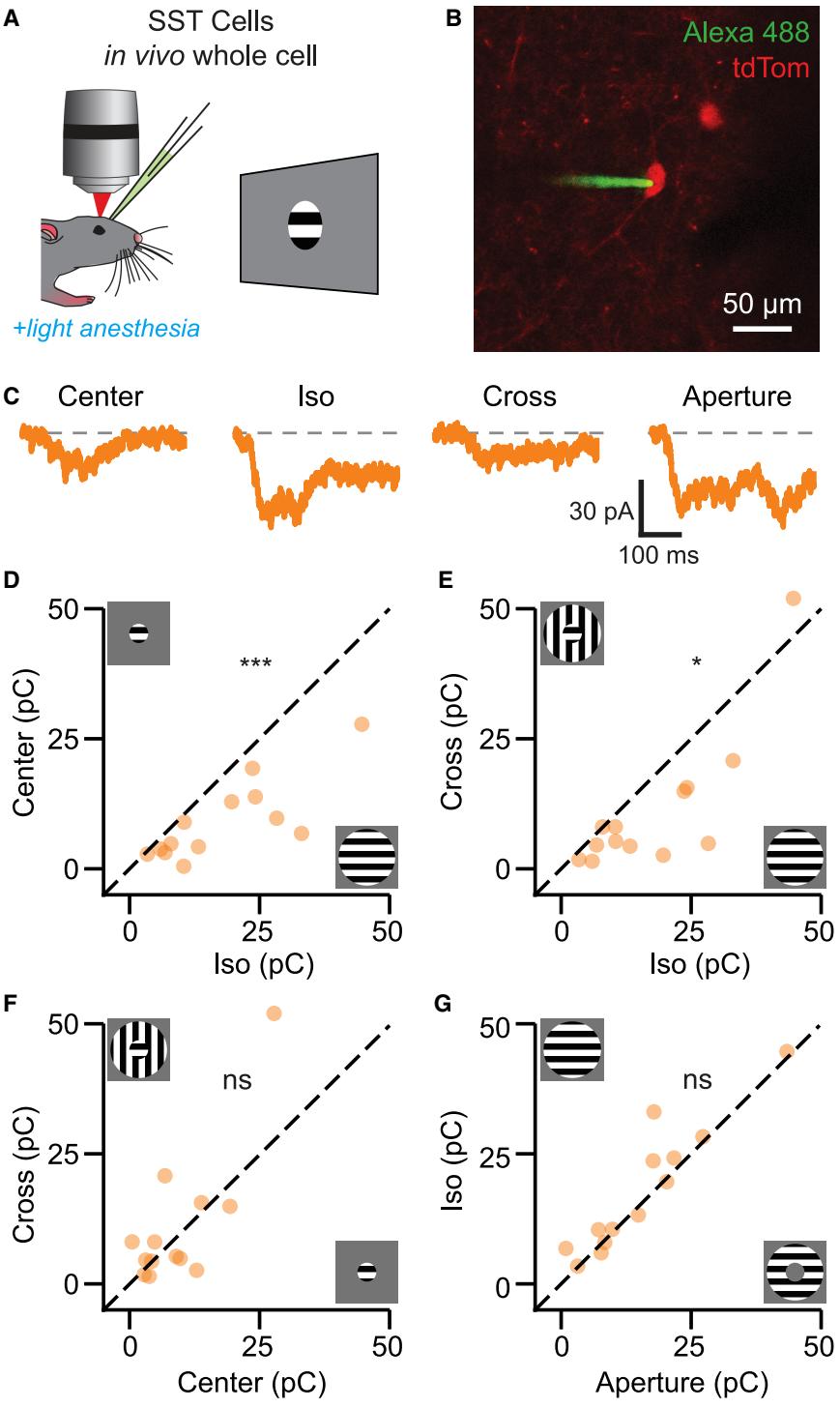

Figure 3. SST cells receive orientation-tuned excitatory input from the retinotopic surround

(A) Schematic of two-photon guided *in vivo* whole-cell voltage-clamp recording of SSTs in lightly anesthetized SST-IRES-Cre;Rosa-LSL-tdTomato mice.

(B) Representative image of a dye-filled patch pipette recording a tdTomato+ SST neuron.

(C) Example of visually evoked synaptic EPSCs from an SST to the indicated visual stimuli. Dashed gray line represents baseline holding potential (−70 mV).

(D) Scatterplots comparing synaptic charge transfer (in pC) of EPSCs in SSTs to center vs. iso stimuli ($n = 13$ cells, $p = 0.00098$, Wilcoxon signed-rank test).

(E) Similar to (D), but comparing cross vs. iso stimuli ($n = 13$ cells, $p = 0.018$, Wilcoxon signed-rank test).

(F) Similar to (D) and (E), but comparing cross vs. center stimuli ($n = 13$ cells, $p = 0.839$, Wilcoxon signed-rank test).

(G) Similar to (D)–(F), but comparing cross vs. aperture stimuli ($n = 13$ cells, $p = 0.188$, Wilcoxon signed-rank test).

See also Figure S4. $^{*}p < 0.05$, $^{***}p < 0.001$; ns, not significant.

also be an alternative mechanism that can explain orientation-dependent surround suppression in V1 L2/3 PCs.

Thus, we sought to test the alternative hypothesis that iso-oriented gratings selectively switch on SSTs by driving substantially more excitation in SSTs than cross-oriented gratings do. We targeted SSTs for whole-cell recordings under 2p guidance in lightly anesthetized mice (see STAR Methods) (Figures 3A and 3B) and probed SSTs' synaptic excitatory input to small gratings, iso-oriented gratings, and cross-oriented gratings. We presented each stimulus across four orientations and focused on the response pattern at each SST's preferred orientation. Consistent with SSTs' well-known spike-rate preference for large compared with small stimuli,[12,14,30,44] large gratings drove substantially more synaptic excitation than did small gratings (Figure 3D), opposite to what we found in PCs (Figure 1). More importantly, we found that SSTs also received substantially more excitation for iso- than cross-oriented gratings (Figure 3E), while cross-oriented gratings drove similar excitation to the center alone (Figure 3F). To test whether SSTs receive additional excitatory input originating from the surround, we compared the response to large gratings to the same stimulus but with the center removed ("aperture gratings"). Remarkably, aperture gratings drove nearly as much excitation as iso-oriented gratings (Figure 3G), implying that a significant component of SSTs' excitatory input can arise from the retinotopic surround, in addition to the input they receive from the center. We note that aperture gratings are thought to engage feedback circuits from higher visual areas,[45] and SSTs are known targets of these projections,[46] but further work would be needed to understand the relative

Please cite this article in press as: Hendricks et al., Feature-tuned synaptic inputs to somatostatin interneurons drive context-dependent processing, Neuron (2025), https://doi.org/10.1016/j.neuron.2025.12.021

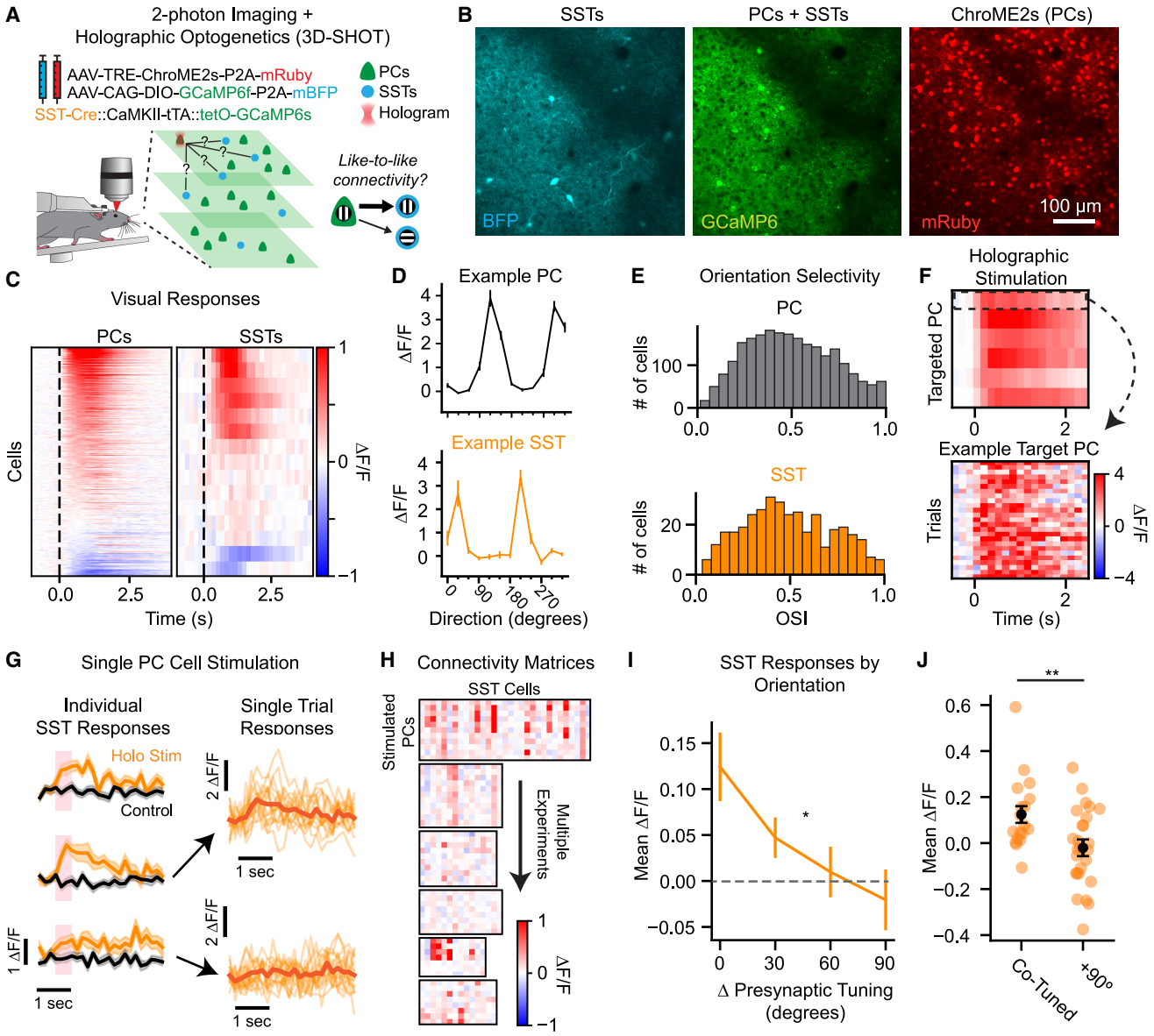

Figure 4. Two-photon optogenetic mapping reveals like-to-like connectivity between PCs and SSTs

(A) Schematic depicting the mapping of functional connectivity between PCs and SSTs with two-photon (2p) holographic optogenetics and calcium imaging. Mice were injected with a viral cocktail that enables Cre-conditional expression of GCaMP6f and BFP in SSTs and TRE-conditional expression of ChroME2s opsin in PCs.

(B) Representative images taken from the same field of view (FOV) of a mouse expressing BFP in SSTs, GCaMP6 in PCs and SSTs, and ChroME2s (mRuby3) in PCs. Scale bar applies to all images.

(C) Example visual responses of PCs (left, n = 368 cells) and SSTs (right, n = 16 cells) to high-contrast, full-screen drifting gratings, taken from a single experimental session. All detected regions of interest (ROIs) in the FOV are plotted.

(D) Representative orientation-tuning curves from PCs (top, black) and SSTs (bottom, orange), taken from a single experimental session.

(E) Histogram of orientation selectivity index (OSI) for PCs (top, gray, n = 2,350 cells) and SSTs (bottom, orange, n = 362 cells).

(F) Average responses of targeted and holographically activated PCs (n = 6 cells) that were stimulated during a single representative experimental session (top). Dashed box on the top row marks the representative cell responses, plotted trial by trial (bottom).

(G) Example calcium traces of three SST cells in response to 2p holographic PC stimulation (left column). Single PCs were optogenetically stimulated with 50 mW of light (red shading). Control trials (black traces, no stimulation) were interleaved with holographic stimulation trials (orange traces). Both average traces (left column) and traces from individual trials (right column) are shown. Average traces (bold orange line) are also overlaid on individual trials (right column).

(H) Connectivity matrices from 6 exemplary experimental sessions. Each pixel represents the mean response of an SST (columns) to holographic stimulation of a stimulated PC (rows). Each box comes from an individual connectivity mapping session (n = 4 mice shown).

(legend continued on next page)

Please cite this article in press as: Hendricks et al., Feature-tuned synaptic inputs to somatostatin interneurons drive context-dependent processing, Neuron (2025), https://doi.org/10.1016/j.neuron.2025.12.021

balance of the input sources of V1 SST neurons. Nonetheless, these measurements of synaptic excitatory input to SSTs provide a clear explanation for why iso-oriented, but not cross-oriented, gratings strongly recruit SST activity.

If SST firing largely originates from the retinotopic surround, then altering the center while keeping the surround constant ("rotated-center" condition) should minimally reduce SSTs' excitatory synaptic input. Indeed, in whole-cell recordings from SSTs, rotating the center of the preferred iso stimulus did not reduce visually evoked synaptic responses (Figure S4A). When the preferred iso stimulus was rotated 90° ("ortho"), synaptic excitation was reduced, and rotating the center of the ortho grating back to the preferred orientation did not increase excitation relative to that generated by the ortho stimulus. Interestingly, this was not entirely reflected in calcium imaging of the suprathreshold activity of SSTs (Figure S4B). In the rotated-center condition, SST visual responses were reduced despite having a preferred surround, suggesting that inhibition from other interneurons may suppress SST firing despite SSTs receiving ample excitation in this condition (Figure S4A). This suppression could come from VIP cells, and, if so, optogenetically silencing VIPs should equalize PC responses between iso and the rotated-center conditions. However, this was not the case: optogenetically silencing VIPs reduced PC responses across all conditions but did not qualitatively restore visual responses to those of the iso condition (Figures S4C and S4D). Thus, VIP inhibition cannot entirely account for the weak firing of SSTs to the rotated center. The remaining difference could be due to inhibition from another interneuron subtype, such as PVs (Figure S4E), or other network dynamics that remain to be fully explored. More generally, contextual modulation was strongest when the center stimulus was aligned to the PC's preferred orientation (Figure S4F), suggesting that feature-dependent connectivity might play a crucial role.

Feature-dependent cortical microcircuitry for figure/ground modulation

What features of the synaptic cortical microarchitecture can explain how SSTs receive more visually evoked excitation for iso- than cross-oriented grating? SSTs receive minimal synaptic input from L4 but substantial excitation from within L2/3.[14,35,47,48] If populations of L2/3 PCs with common orientation tuning converge onto individual SSTs,[43] this would explain why they receive more synaptic excitation for iso-oriented gratings than for other stimuli. Thus, we hypothesized that lateral input within L2/3 between PCs and SSTs should be "like-to-like" in orientation space; that is, PCs should selectively drive SSTs with common orientation preferences. To test this, we used 2p holographic optogenetics (see STAR Methods) to photo-activate individual orientation-tuned PCs while performing simultaneous 2p calcium imaging of PCs and SSTs expressing GCaMP6 (Figure 4A). We conditionally expressed ChroME2s[49] in PCs for photostimulation, along with blue fluorescent protein (BFP), to positively identify SSTs post hoc (Figure 4B). First, we confirmed that we could robustly drive visual responses in both PCs and SSTs (Figure 4C) and then mapped the orientation tuning of PCs and SSTs using full-screen high-contrast drifting gratings (Figures 4D and 4E). Then, we confirmed the efficacy of photostimulating PCs using targeted holographic illumination (Figure 4F). Finally, we photo-activated a sequence of individual PCs while monitoring the somatic calcium activity of nearby SSTs (Figures 4G and 4H). Consistent with our switch-on hypothesis, the shared orientation preference of PCs and SSTs strongly predicted their functional connectivity: co-tuned PCs drove substantial activation of SSTs, while orthogonally tuned PCs drove slight suppression (Figures 4I and 4J). Although single-cell stimulation is not an activity pattern ever driven by visual stimuli, it is helpful for identifying putative synaptic coupling between specific neurons.[4] To approximate more physiological conditions, we constructed ensembles with varying numbers of targeted PCs. SST responses increased with ensemble size (Figure S5). These results provide the first demonstration of a like-to-like circuit motif between cortical excitatory neurons and SSTs. Taken together, our data provide a clear mechanism that connects precise patterns of synaptic connectivity in V1 to recurrent circuit dynamics that help mediate higher-order contextual computations.

DISCUSSION

Our approach for probing the synaptic and circuit logic of figure/ground modulation reveals previously unknown functional principles of cortical wiring and provides a detailed mechanistic model of a cortically emergent computation. Based on these experiments, we propose a conceptual model to explain figure/ground modulation: iso-oriented stimuli drive co-tuned PCs across the retinotopic map in the visual cortex, and these co-tuned PCs selectively converge onto individual SSTs, causing them to selectively respond to iso-oriented, but not cross-oriented, stimuli. In turn, this population of co-tuned SSTs inhibits PCs (as well as PVs and VIPs), suppressing total synaptic activity and network firing rates in the absence of a perceptual figure (Figure 5A). PCs also receive less somatic inhibition from PVs due to this SST-mediated suppression, resulting in a net decrease of both excitation and somatic inhibition.[37] Conversely, cross-oriented stimuli drive orthogonally tuned pools of PCs between the retinotopic center and surround, and, as a consequence, SSTs receive less overall excitation and fire much less when the image contains a perceptual figure. This prevents network suppression by SSTs and results in stronger overall V1 activity (Figure 5B), despite PCs receiving more somatic inhibition from PVs. These high firing rates presumably help define the existence of specific figural objects in the scene. Inhibition from VIPs onto SSTs, specifically for

(I) Quantification of SST responses (mean ΔF/F) during 2p holographic stimulation of putative pre-synaptic PCs, sorted by their relative difference in orientation (in °) to stimulated PCs (n = 120 total tested PC-SST pairs, 7 sessions, 4 mice, p = 0.0247, Kruskal-Wallis H test).

(J) Similar to (I), except only plotting the individual responses of SSTs that are either co-tuned or orthogonally tuned (Δ +90°) with stimulated PCs (co-tuned, n = 18 PC-SST pairs; +90°, n = 26 PC-SST pairs, p = 0.00674, Mann-Whitney U test). Data are presented as mean ± SEM unless otherwise noted.

See also Figure S5. *p < 0.05, **p < 0.01.

Please cite this article in press as: Hendricks et al., Feature-tuned synaptic inputs to somatostatin interneurons drive context-dependent processing, Neuron (2025), https://doi.org/10.1016/j.neuron.2025.12.021

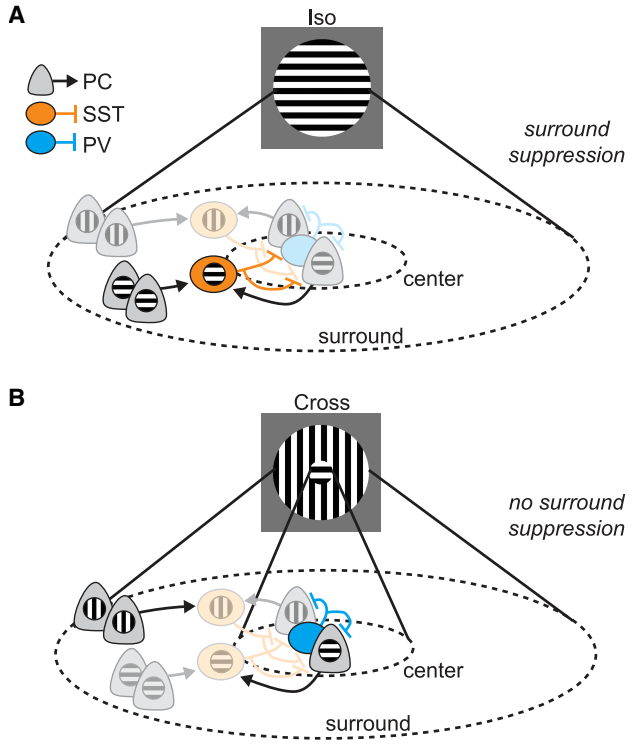

Figure 5. Like-to-like functional connectivity model for orientation-dependent surround suppression

(A) Tuned (like-to-like) PC→SST connections from both the center and surround combine and sufficiently increase SST activity, driving surround suppression to iso gratings in PCs. PVs are also suppressed by SST cell firing. Grays, oranges, and blues represent PC, SST, and PV cells and connections, respectively. Some connections are omitted for clarity. Shading represents relative activity of cells and connections (arrows). Light shading represents present, but not active, connections and cells. Darker shading represents present and active connections and cells. Center and surround receptive fields are indicated by dashed lines. Oriented gratings within PCs and SSTs depict their preferred orientation.

(B) For cross-oriented gratings, surround PCs and center PCs drive synaptic input into 2 different populations of SSTs but not enough to sufficiently increase SST activity for surround suppression. PVs are also no longer suppressed by SSTs.

figure-containing stimuli,[11,12] may still serve to enhance the consequences of feature-dependent excitatory wiring between PCs and SSTs.

Although we did not observe the same degree of response facilitation to cross-oriented gratings (compared with center-only gratings) as previous studies (possibly due to differences in specific parameters of the visual stimuli),[12] such facilitation may not be required for perceptual phenomena such as figure/ground segregation. Instead, a simple difference in the firing rates of PCs when encoding the figure versus the background might be sufficient. In our experiments, some PCs were facilitated while others were slightly suppressed when adding a cross-oriented background to a center stimulus (Figure 1). On average, there was a slight suppression across the whole population, although this suppression was much less than when the surround was iso-oriented to the center. The net consequence of the synaptic microarchitecture described here may be one of the first physiological steps in figure/ground modulation.

SSTs' synaptic input largely, but not exclusively, appears to originate from the retinotopic surround (Figure 3). In fact, in our conceptual model (Figure 5), SSTs require input from both co-tuned PCs in the surround and the center to drive surround suppression. Removing either would result in the loss of SST firing, such as in the case of orientation-tuned surround suppression. Although rotating the center alone did not reduce excitatory input in SSTs, it did reduce their suprathreshold responses, an effect that could not be attributed to VIPs (Figure S4). These rotated-center stimuli also revealed that orientation-tuned surround suppression in PCs was dependent on the alignment of the center with its preferred orientation. This pattern is consistent with classical studies in cats and monkeys, where cross-oriented surround stimuli relieve surround suppression at their preferred stimulus,[50] while cross-oriented stimuli within the CRF lack this orientation dependence.[22] Notably, cross-oriented stimuli of any orientation drove PV activity, and thereby PV→SST suppression could at least partially account for this apparent mismatch between SST synaptic input and firing in the rotated-center condition. Other sources of inhibition, the precise timing of excitatory input relative to inhibitory input, or features of network dynamics, might also contribute. Cross stimuli may also drive shunting inhibition onto SSTs through VIPs, manifesting as a loss of voltage-clamped synaptic excitation. Changes in PC firing may also result from other network dynamics, such as surround suppression of afferent PCs, which we did not test in our set of experiments.

In our experiments, we primarily mapped functional connectivity from single PCs to SSTs to simplify the analysis. We observed recruitment of SSTs even when stimulating single PCs, consistent with brain slice paired-patch experiments,[51] where activation of a single PC can recruit SST firing and generate suppression in other PCs. When we activated larger ensembles of PCs, which would be closer to physiological conditions during visual stimulation, we observed a substantial increase in SST recruitment, which is also consistent with results in brain slices when stimulating multiple PCs.[51,52]

Because the basic features of cortical architecture are preserved across widely different cortical areas,[53,54] our work raises the notion that feature-specific lateral wiring from PCs to SSTs might generally be involved in higher-order cortical computations. SSTs also derive substantial input from top-down feedback pathways from higher cortical areas,[46,55–58] where excitatory neurons often show more integrative properties.[59] Suppressing top-down feedback both reduces surround suppression across multiple species and can also reduce its orientation dependence.[11,60–62] This suggests that excitatory feedback to V1 SSTs might also obey a like-to-like rule. So far, we lack the tools to map the feature dependence of functional connectivity between distant excitatory neurons and SSTs or any other cell types. However, this may be possible with recent advances in very large field-of-view 2p imaging and 2p optogenetic platforms[63] or through a combination of transsynaptic tracing strategies[6,10,64] and optogenetic perturbations. Moreover, although the increasingly well-characterized VIP disinhibitory

Please cite this article in press as: Hendricks et al., Feature-tuned synaptic inputs to somatostatin interneurons drive context-dependent processing, Neuron (2025), https://doi.org/10.1016/j.neuron.2025.12.021

circuit[12,33,65,66] is not required for setting up the computation we study here, it likely acts as a potent brain-state or context-dependent modulator that could scale the gain of the feature-selective PC→SST circuit to match ongoing behavioral demands.[30,65,66] As the cortical neuromodulatory state can control the dynamics of synapses between PCs and SSTs,[67] it is possible that VIPs play a more crucial role when the excitatory synaptic gain onto SSTs changes across different behavioral states.

We note that our conceptual model (Figure 5) does not require like-to-like connectivity from SST→PC, although it does not exclude it. If SSTs broadly synapse onto PCs without respect to their shared tuning preferences, orientation-dependent surround suppression will still arise if SST firing requires the conjunction of synaptic input from both surround and center PCs that are co-tuned to the SST. In this scenario, different pools of orientation-tuned SSTs fire for different orientations of the background iso-oriented stimulus, but for a cross-oriented stimulus, few, if any, SSTs are strongly recruited, consistent with our observation that SSTs receive strong synaptic input from the surround (Figure 3). Although "like-to-like-to-like" functional connectivity in the PC→SST→PC pathway may not be necessary, it might reinforce orientation-dependent surround suppression that is initially set up by the patterns of excitatory synaptic input to SSTs that we described here. Further experiments mapping the SST→PC functional connectivity pattern will help elucidate the circuit motifs that support orientation-dependent surround suppression, and other results point in this direction.[68]

PVs, together with SSTs, cooperatively regulate the net inhibitory tone onto PCs[69,70] and thereby shape visual responses in V1. Similar to PCs, PVs strongly prefer cross-oriented gratings (Figure S1) and receive monosynaptic inhibition from SSTs.[33,35] In this model, SSTs directly suppress PCs while simultaneously reducing PV-mediated somatic inhibition. This is consistent with our findings that PCs receive less synaptic inhibition (measured at the soma) to iso-oriented gratings despite high SST activity (Figure 1). This should be partially explained by somatic patch electrodes better recovering inhibitory inputs near the soma (closer to PV input synapses) than in the dendrites (closer to SST input synapses).[37] Moreover, silencing SSTs increased FS unit (putative PV) activity (Figure S2), an effect that is accompanied by an increase in somatically measured synaptic inhibition onto PCs.[37] Although not tested here, a like-to-like connectivity motif is unlikely to emerge at the SST→PV synapse given the relatively weak orientation tuning of PVs.[71,72]

Contextual modulation includes other key computations beyond figure/ground modulation. The visual system must also address sensory ambiguities due to occlusion, low contrast, variable reflectance, etc., to identify objects. Top-down feedback circuits,[45,57,58,73] together with lateral connections within V1,[11,12,34,35] might address all of these challenging sensory contexts through precise patterns of synaptic connectivity between excitatory and specific subtypes of inhibitory interneurons. Other sensory cortical areas, and even higher cortical regions, contain similar sets of cell types with potentially similar patterns of connectivity.[40,53,54,74–76] Thus, it may be possible that other cortical areas might repeatedly exploit the like-to-like PC→SST circuitry we discovered here to implement contextual processing in other feature spaces. Defects in these circuits might help explain features of complex cognitive or neurological disorders.

RESOURCE AVAILABILITY

Lead contact

Requests for further information and resources should be directed to, and will be fulfilled by, the lead contact, Hillel Adesnik (hadesnik@berkeley.edu).

Materials availability

All animal strains used in this study are available from Jackson Laboratories. Viral vectors generated for this study can be obtained from the lead contact upon request.

Data and code availability

- Data have been deposited at Zenodo and are publicly available as of the date of publication at https://10.5281/zenodo.17527499.
- All original code has been deposited at Zenodo and is publicly available as of the date of publication at https://10.5281/zenodo.17527499. It is also available at https://github.com/willyh101/iso-cross.
- Any additional information required to reanalyze the data reported in this paper is available from the lead contact upon request.

ACKNOWLEDGMENTS

This work was supported by the National Institutes of Health (NIH) grants F32-EY031977 (W.D.H.), F32-EY034022 (M.S.), and R01-EY023756 and U19NS107613 (H.A.). J.V. was supported by grants from the Swiss National Foundation (P300PA_164719 and P2FRP3_155172) and the DFG (VE 938/2-1 and INST 39/1422-1). This content is solely the responsibility of the authors and does not necessarily represent the views of the National Institutes of Health. We thank Janine Beyer, Karthika Gopakumar, and Savitha Sridharan for technical support.

AUTHOR CONTRIBUTIONS

All authors conceived of the study. H.A. and W.D.H. wrote the manuscript. W.D.H. performed all 2p holographic optogenetics experiments. H.A. performed *in vivo* whole-cell recordings from PCs. J.V. performed all extracellular multi-electrode array physiology and one-photon optogenetics. D.M. performed all 2p calcium imaging with one-photon optogenetics. M.S. performed all targeted 2p patch-clamp experiments. W.D.H. prepared all figures and performed all statistical analyses.

DECLARATION OF INTERESTS

H.A. has a patent related to the technology used in this publication: three-dimensional scanless holographic optogenetics with temporal focusing, patent #US20190227490A1, L. Waller, H. Adesnik, N. Pegard.

STAR★METHODS

Detailed methods are provided in the online version of this paper and include the following:

- KEY RESOURCES TABLE
- EXPERIMENTAL MODEL AND STUDY PARTICIPANT DETAILS
- METHOD DETAILS
  - Viral injections
  - Electrophysiology
  - One-photon optogenetics
  - Two-photon holographic optogenetics

SUPPLEMENTAL INFORMATION

Supplemental information can be found online at https://doi.org/10.1016/j.neuron.2025.12.021.

Received: April 4, 2025
Revised: September 23, 2025
Accepted: December 16, 2025

REFERENCES

1. Ko, H., Hofer, S.B., Pichler, B., Buchanan, K.A., Sjöström, P.J., and Mrsic-Flogel, T.D. (2011). Functional specificity of local synaptic connections in neocortical networks. Nature *473*, 87–91. https://doi.org/10.1038/nature09880.
2. The MICrONS Consortium (2025). Functional connectomics spanning multiple areas of mouse visual cortex. Nature *640*, 435–447. https://doi.org/10.1038/s41586-025-08790-w.
3. Oldenburg, I.A., Hendricks, W.D., Handy, G., Shamardani, K., Bounds, H.A., Doiron, B., and Adesnik, H. (2024). The logic of recurrent circuits in the primary visual cortex. Nat. Neurosci. *27*, 137–147. https://doi.org/10.1038/s41593-023-01510-5.
4. Chettih, S.N., and Harvey, C.D. (2019). Single-neuron perturbations reveal feature-specific competition in V1. Nature *567*, 334–340. https://doi.org/10.1038/s41586-019-0997-6.
5. Cossell, L., Iacaruso, M.F., Muir, D.R., Houlton, R., Sader, E.N., Ko, H., Hofer, S.B., and Mrsic-Flogel, T.D. (2015). Functional organization of excitatory synaptic strength in primary visual cortex. Nature *518*, 399–403. https://doi.org/10.1038/nature14182.
6. Rossi, L.F., Harris, K.D., and Carandini, M. (2020). Spatial connectivity matches direction selectivity in visual cortex. Nature *588*, 648–652. https://doi.org/10.1038/s41586-020-2894-4.
7. Marshel, J.H., Kim, Y.S., Machado, T.A., Quirin, S., Benson, B., Kadmon, J., Raja, C., Chibukhchyan, A., Ramakrishnan, C., Inoue, M., et al. (2019). Cortical layer–specific critical dynamics triggering perception. Science *365*, eaaw5202. https://doi.org/10.1126/science.aaw5202.
8. Lien, A.D., and Scanziani, M. (2013). Tuned thalamic excitation is amplified by visual cortical circuits. Nat. Neurosci. *16*, 1315–1323. https://doi.org/10.1038/nn.3488.
9. Bock, D.D., Lee, W.-C.A., Kerlin, A.M., Andermann, M.L., Hood, G., Wetzel, A.W., Yurgenson, S., Soucy, E.R., Kim, H.S., and Reid, R.C. (2011). Network anatomy and in vivo physiology of visual cortical neurons. Nature *471*, 177–182. https://doi.org/10.1038/nature09802.
10. Wertz, A., Trenholm, S., Yonehara, K., Hillier, D., Raics, Z., Leinweber, M., Szalay, G., Ghanem, A., Keller, G., Rózsa, B., et al. (2015). Single-cell-initiated monosynaptic tracing reveals layer-specific cortical network modules. Science *349*, 70–74. https://doi.org/10.1126/science.aab1687.
11. Kirchberger, L., Mukherjee, S., Schnabel, U.H., van Beest, E.H., Barsegyan, A., Levelt, C.N., Heimel, J.A., Lorteije, J.A.M., van der Togt, C., Self, M.W., et al. (2021). The essential role of recurrent processing for figure-ground perception in mice. Sci. Adv. *7*, eabe1833. https://doi.org/10.1126/sciadv.abe1833.
12. Keller, A.J., Dipoppa, M., Roth, M.M., Caudill, M.S., Ingrosso, A., Miller, K.D., and Scanziani, M. (2020). A Disinhibitory Circuit for Contextual Modulation in Primary Visual Cortex. Neuron *108*, 1181–1193.e8. https://doi.org/10.1016/j.neuron.2020.11.013.
13. Millman, D.J., Ocker, G.K., Caldejon, S., Kato, I., Larkin, J.D., Lee, E.K., Luviano, J., Nayan, C., Nguyen, T.V., North, K., et al. (2020). VIP interneurons in mouse primary visual cortex selectively enhance responses to weak but specific stimuli. eLife *9*, e55130. https://doi.org/10.7554/eLife.55130.
14. Adesnik, H., Bruns, W., Taniguchi, H., Huang, Z.J., and Scanziani, M. (2012). A neural circuit for spatial summation in visual cortex. Nature *490*, 226–231. https://doi.org/10.1038/nature11526.
15. Nienborg, H., Hasenstaub, A., Nauhaus, I., Taniguchi, H., Huang, Z.J., and Callaway, E.M. (2013). Contrast dependence and differential contributions from somatostatin- and parvalbumin-expressing neurons to spatial integration in mouse V1. J. Neurosci. *33*, 11145–11154. https://doi.org/10.1523/JNEUROSCI.5320-12.2013.
16. Lamme, V.A. (1995). The neurophysiology of figure-ground segregation in primary visual cortex. J. Neurosci. *15*, 1605–1615. https://doi.org/10.1523/JNEUROSCI.15-02-01605.1995.
17. Schnabel, U.H., Bossens, C., Lorteije, J.A.M., Self, M.W., Op de Beeck, H., and Roelfsema, P.R. (2018). Figure-ground perception in the awake mouse and neuronal activity elicited by figure-ground stimuli in primary visual cortex. Sci. Rep. *8*, 17800. https://doi.org/10.1038/s41598-018-36087-8.
18. Zipser, K., Lamme, V.A., and Schiller, P.H. (1996). Contextual modulation in primary visual cortex. J. Neurosci. *16*, 7376–7389. https://doi.org/10.1523/JNEUROSCI.16-22-07376.1996.
19. Knierim, J.J., and van Essen, D.C. (1992). Neuronal responses to static texture patterns in area V1 of the alert macaque monkey. J. Neurophysiol. *67*, 961–980. https://doi.org/10.1152/jn.1992.67.4.961.
20. Self, M.W., Lorteije, J.A.M., Vangeneugden, J., van Beest, E.H., Grigore, M.E., Levelt, C.N., Heimel, J.A., and Roelfsema, P.R. (2014). Orientation-Tuned Surround Suppression in Mouse Visual Cortex. J. Neurosci. *34*, 9290–9304. https://doi.org/10.1523/JNEUROSCI.5051-13.2014.
21. Shushruth, S., Nurminen, L., Bijanzadeh, M., Ichida, J.M., Vanni, S., and Angelucci, A. (2013). Different orientation tuning of near- and far-surround suppression in macaque primary visual cortex mirrors their tuning in human perception. J. Neurosci. *33*, 106–119. https://doi.org/10.1523/JNEUROSCI.2518-12.2013.
22. Sillito, A.M., Grieve, K.L., Jones, H.E., Cudeiro, J., and Davis, J. (1995). Visual cortical mechanisms detecting focal orientation discontinuities. Nature *378*, 492–496. https://doi.org/10.1038/378492a0.
23. Coen-Cagli, R., Kohn, A., and Schwartz, O. (2015). Flexible gating of contextual influences in natural vision. Nat. Neurosci. *18*, 1648–1655. https://doi.org/10.1038/nn.4128.
24. Polat, U., Mizobe, K., Pettet, M.W., Kasamatsu, T., and Norcia, A.M. (1998). Collinear stimuli regulate visual responses depending on cell's contrast threshold. Nature *391*, 580–584. https://doi.org/10.1038/35372.
25. Blakemore, C., and Tobin, E.A. (1972). Lateral inhibition between orientation detectors in the cat's visual cortex. Exp. Brain Res. *15*, 439–440. https://doi.org/10.1007/BF00234129.
26. Bair, W., Cavanaugh, J.R., and Movshon, J.A. (2003). Time course and time-distance relationships for surround suppression in macaque V1 neurons. J. Neurosci. *23*, 7690–7701. https://doi.org/10.1523/JNEUROSCI.23-20-07690.2003.
27. Cavanaugh, J.R., Bair, W., and Movshon, J.A. (2002). Nature and interaction of signals from the receptive field center and surround in macaque V1 neurons. J. Neurophysiol. *88*, 2530–2546. https://doi.org/10.1152/jn.00692.2001.
28. Blakemore, C., Carpenter, R.H.S., and Georgeson, M.A. (1970). Lateral Inhibition between Orientation Detectors in the Human Visual System. Nature *228*, 37–39. https://doi.org/10.1038/228037a0.
29. Li, Z. (1999). Visual segmentation by contextual influences via intracortical interactions in the primary visual cortex. Network *10*, 187–212. https://doi.org/10.1088/0954-898X_10_2_305.
30. Dipoppa, M., Ranson, A., Krumin, M., Pachitariu, M., Carandini, M., and Harris, K.D. (2018). Vision and locomotion shape the interactions between

neuron types in mouse visual cortex. Neuron *98*, 602–615.e8. https://doi.org/10.1016/j.neuron.2018.03.037.

31. Veit, J., Hakim, R., Jadi, M.P., Sejnowski, T.J., and Adesnik, H. (2017). Cortical gamma band synchronization through somatostatin interneurons. Nat. Neurosci. *20*, 951–959. https://doi.org/10.1038/nn.4562.
32. Jiang, X., Shen, S., Cadwell, C.R., Berens, P., Sinz, F., Ecker, A.S., Patel, S., and Tolias, A.S. (2015). Principles of connectivity among morphologically defined cell types in adult neocortex. Science *350*, aac9462. https://doi.org/10.1126/science.aac9462.
33. Pfeffer, C.K., Xue, M., He, M., Huang, Z.J., and Scanziani, M. (2013). Inhibition of inhibition in visual cortex: the logic of connections between molecularly distinct interneurons. Nat. Neurosci. *16*, 1068–1076. https://doi.org/10.1038/nn.3446.
34. Hage, T.A., Bosma-Moody, A., Baker, C.A., Kratz, M.B., Campagnola, L., Jarsky, T., Zeng, H., and Murphy, G.J. (2022). Synaptic connectivity to L2/3 of primary visual cortex measured by two-photon optogenetic stimulation. eLife *11*, e71103. https://doi.org/10.7554/eLife.71103.
35. Campagnola, L., Seeman, S.C., Chartrand, T., Kim, L., Hoggarth, A., Gamlin, C., Ito, S., Trinh, J., Davoudian, P., Radaelli, C., et al. (2022). Local connectivity and synaptic dynamics in mouse and human neocortex. Science *375*, eabj5861. https://doi.org/10.1126/science.abj5861.
36. Fino, E., and Yuste, R. (2011). Dense inhibitory connectivity in neocortex. Neuron *69*, 1188–1203. https://doi.org/10.1016/j.neuron.2011.02.025.
37. Adesnik, H. (2017). Synaptic Mechanisms of Feature Coding in the Visual Cortex of Awake Mice. Neuron *95*, 1147–1159.e4. https://doi.org/10.1016/j.neuron.2017.08.014.
38. Rubin, D.B., Van Hooser, S.D., and Miller, K.D. (2015). The Stabilized Supralinear Network: A Unifying Circuit Motif Underlying Multi-Input Integration in Sensory Cortex. Neuron *85*, 402–417. https://doi.org/10.1016/j.neuron.2014.12.026.
39. Ozeki, H., Finn, I.M., Schaffer, E.S., Miller, K.D., and Ferster, D. (2009). Inhibitory Stabilization of the Cortical Network Underlies Visual Surround Suppression. Neuron *62*, 578–592. https://doi.org/10.1016/j.neuron.2009.03.028.
40. Lee, S., Kruglikov, I., Huang, Z.J., Fishell, G., and Rudy, B. (2013). A disinhibitory circuit mediates motor integration in the somatosensory cortex. Nat. Neurosci. *16*, 1662–1670. https://doi.org/10.1038/nn.3544.
41. Fu, Y., Tucciarone, J.M., Espinosa, J.S., Sheng, N., Darcy, D.P., Nicoll, R.A., Huang, Z.J., and Stryker, M.P. (2014). A cortical circuit for gain control by behavioral state. Cell *156*, 1139–1152. https://doi.org/10.1016/j.cell.2014.01.050.
42. Pi, H.-J., Hangya, B., Kvitsiani, D., Sanders, J.I., Huang, Z.J., and Kepecs, A. (2013). Cortical interneurons that specialize in disinhibitory control. Nature *503*, 521–524. https://doi.org/10.1038/nature12676.
43. Ma, W.P., Liu, B.H., Li, Y.T., Huang, Z.J., Zhang, L.I., and Tao, H.W. (2010). Visual Representations by Cortical Somatostatin Inhibitory Neurons—Selective But with Weak and Delayed Responses. J. Neurosci. *30*, 14371–14379. https://doi.org/10.1523/JNEUROSCI.3248-10.2010.
44. Mossing, D.P., Veit, J., Palmigiano, A., Miller, K.D., and Adesnik, H. (2021). Antagonistic inhibitory subnetworks control cooperation and competition across cortical space. Preprint at bioRxiv. https://doi.org/10.1101/2021.03.31.437953.
45. Keller, A.J., Roth, M.M., and Scanziani, M. (2020). Feedback generates a second receptive field in neurons of the visual cortex. Nature *582*, 545–549. https://doi.org/10.1038/s41586-020-2319-4.
46. Shen, S., Jiang, X., Scala, F., Fu, J., Fahey, P., Kobak, D., Tan, Z., Zhou, N., Reimer, J., Sinz, F., et al. (2022). Distinct organization of two corticocortical feedback pathways. Nat. Commun. *13*, 6389. https://doi.org/10.1038/s41467-022-33883-9.
47. Chou, C.Y.C., Wong, H.H.W., Guo, C., Boukoulou, K.E., Huang, C., Jannat, J., Klimenko, T., Li, V.Y., Liang, T.A., Wu, V.C., et al. (2025). Principles of visual cortex excitatory microcircuit organization. Innovation (Camb.) *6*, 100735. https://doi.org/10.1016/j.xinn.2024.100735.
48. Naka, A., Veit, J., Shababo, B., Chance, R.K., Risso, D., Stafford, D., Snyder, B., Egladyous, A., Chu, D., Sridharan, S., et al. (2019). Complementary networks of cortical somatostatin interneurons enforce layer specific control. eLife *8*, e43696. https://doi.org/10.7554/eLife.43696.
49. Sridharan, S., Gajowa, M.A., Ogando, M.B., Jagadisan, U.K., Abdeladim, L., Sadahiro, M., Bounds, H.A., Hendricks, W.D., Turney, T.S., Tayler, I., et al. (2022). High-performance microbial opsins for spatially and temporally precise perturbations of large neuronal networks. Neuron *110*, 1139–1155.e6. https://doi.org/10.1016/j.neuron.2022.01.008.
50. Shushruth, S., Mangapathy, P., Ichida, J.M., Bressloff, P.C., Schwabe, L., and Angelucci, A. (2012). Strong recurrent networks compute the orientation tuning of surround modulation in the primate primary visual cortex. J. Neurosci. *32*, 308–321. https://doi.org/10.1523/JNEUROSCI.3789-11.2012.
51. Kapfer, C., Glickfeld, L.L., Atallah, B.V., and Scanziani, M. (2007). Supralinear increase of recurrent inhibition during sparse activity in the somatosensory cortex. Nat. Neurosci. *10*, 743–753. https://doi.org/10.1038/nn1909.
52. Silberberg, G., and Markram, H. (2007). Disynaptic inhibition between neocortical pyramidal cells mediated by Martinotti cells. Neuron *53*, 735–746. https://doi.org/10.1016/j.neuron.2007.02.012.
53. Harris, K.D., and Mrsic-Flogel, T.D. (2013). Cortical connectivity and sensory coding. Nature *503*, 51–58. https://doi.org/10.1038/nature12654.
54. Douglas, R.J., and Martin, K.A.C. (2004). Neuronal circuits of the neocortex. Annu. Rev. Neurosci. *27*, 419–451. https://doi.org/10.1146/annurev.neuro.27.070203.144152.
55. Yao, S., Wang, Q., Hirokawa, K.E., Ouellette, B., Ahmed, R., Bomben, J., Brouner, K., Casal, L., Caldejon, S., Cho, A., et al. (2023). A whole-brain monosynaptic input connectome to neuron classes in mouse visual cortex. Nat. Neurosci. *26*, 350–364. https://doi.org/10.1038/s41593-022-01219-x.
56. Wall, N.R., De La Parra, M., Sorokin, J.M., Taniguchi, H., Huang, Z.J., and Callaway, E.M. (2016). Brain-wide maps of synaptic input to cortical interneurons. J. Neurosci. *36*, 4000–4009. https://doi.org/10.1523/JNEUROSCI.3967-15.2016.
57. Zhang, S., Xu, M., Kamigaki, T., Hoang Do, J.P.H., Chang, W.-C., Jenvay, S., Miyamichi, K., Luo, L., and Dan, Y. (2014). Selective attention. Long-range and local circuits for top-down modulation of visual cortex processing. Science *345*, 660–665. https://doi.org/10.1126/science.1254126.
58. Li, J.Y., Hass, C.A., Matthews, I., Kristl, A.C., and Glickfeld, L.L. (2021). Distinct recruitment of feedforward and recurrent pathways across higher-order areas of mouse visual cortex. Curr. Biol. *31*, 5024–5036.e5. https://doi.org/10.1016/j.cub.2021.09.042.
59. Murgas, K.A., Wilson, A.M., Michael, V., and Glickfeld, L.L. (2020). Unique spatial integration in mouse primary visual cortex and higher visual areas. J. Neurosci. *40*, 1862–1873. https://doi.org/10.1523/JNEUROSCI.1997-19.2020.
60. Nassi, J.J., Lomber, S.G., and Born, R.T. (2013). Corticocortical feedback contributes to surround suppression in V1 of the alert primate. J. Neurosci. *33*, 8504–8517. https://doi.org/10.1523/JNEUROSCI.5124-12.2013.
61. Vangeneugden, J., van Beest, E.H., Cohen, M.X., Lorteije, J.A.M., Mukherjee, S., Kirchberger, L., Montijn, J.S., Thamizharasu, P., Camillo, D., Levelt, C.N., et al. (2019). Activity in lateral visual areas contributes to surround suppression in awake mouse V1. Curr. Biol. *29*, 4268–4275.e7. https://doi.org/10.1016/j.cub.2019.10.037.
62. Nurminen, L., Merlin, S., Bijanzadeh, M., Federer, F., and Angelucci, A. (2018). Top-down feedback controls spatial summation and response amplitude in primate visual cortex. Nat. Commun. *9*, 2281. https://doi.org/10.1038/s41467-018-04500-5.
63. Abdeladim, L., Jagadisan, U.K., Shin, H., Ogando, M.B., and Adesnik, H. (2025). Probing inter-areal computations with a cellular resolution two-photon holographic mesoscope. Preprint at bioRxiv. https://doi.org/10.1101/2023.03.02.530875.

64. Wickersham, I.R., Lyon, D.C., Barnard, R.J.O., Mori, T., Finke, S., Conzelmann, K.-K., Young, J.A.T., and Callaway, E.M. (2007). Monosynaptic restriction of transsynaptic tracing from single, genetically targeted neurons. Neuron *53*, 639–647. https://doi.org/10.1016/j.neuron.2007.01.033.

65. Pakan, J.M., Lowe, S.C., Dylda, E., Keemink, S.W., Currie, S.P., Coutts, C.A., and Rochefort, N.L. (2016). Behavioral-state modulation of inhibition is context-dependent and cell type specific in mouse visual cortex. eLife *5*, e14985. https://doi.org/10.7554/eLife.14985.

66. Ferguson, K.A., Salameh, J., Alba, C., Selwyn, H., Barnes, C., Lohani, S., and Cardin, J.A. (2023). VIP interneurons regulate cortical size tuning and visual perception. Cell Rep. *42*, 113088. https://doi.org/10.1016/j.celrep.2023.113088.

67. Urban-Ciecko, J., Jouhanneau, J.-S., Myal, S.E., Poulet, J.F.A., and Barth, A.L. (2018). Precisely timed nicotinic activation drives SST inhibition in neocortical circuits. Neuron *97*, 611–625.e5. https://doi.org/10.1016/j.neuron.2018.01.037.

68. Ogando, M.B., Abdeladim, L., Sit, K.K., Shin, H., Sridharan, S., Gopakumar, K., and Adesnik, H. (2025). Feature-specific inhibitory connectivity augments the accuracy of cortical representations. Preprint at bioRxiv. https://doi.org/10.1101/2025.08.02.668307.

69. Rikhye, R.V., Yildirim, M., Hu, M., Breton-Provencher, V., and Sur, M. (2021). Reliable sensory processing in mouse visual cortex through cooperative interactions between somatostatin and parvalbumin interneurons. J. Neurosci. *41*, 8761–8778. https://doi.org/10.1523/JNEUROSCI.3176-20.2021.

70. Karnani, M.M., Jackson, J., Ayzenshtat, I., Tucciarone, J., Manoocheri, K., Snider, W.G., and Yuste, R. (2016). Cooperative Subnetworks of Molecularly Similar Interneurons in Mouse Neocortex. Neuron *90*, 86–100. https://doi.org/10.1016/j.neuron.2016.02.037.

71. Kerlin, A.M., Andermann, M.L., Berezovskii, V.K., and Reid, R.C. (2010). Broadly tuned response properties of diverse inhibitory neuron subtypes in mouse visual cortex. Neuron *67*, 858–871. https://doi.org/10.1016/j.neuron.2010.08.002.

72. Atallah, B.V., Bruns, W., Carandini, M., and Scanziani, M. (2012). Parvalbumin-expressing interneurons linearly transform cortical responses to visual stimuli. Neuron *73*, 159–170. https://doi.org/10.1016/j.neuron.2011.12.013.

73. Klink, P.C., Dagnino, B., Gariel-Mathis, M.-A., and Roelfsema, P.R. (2017). Distinct feedforward and feedback effects of microstimulation in visual cortex reveal neural mechanisms of texture segregation. Neuron *95*, 209–220.e3. https://doi.org/10.1016/j.neuron.2017.05.033.

74. Tasic, B., Yao, Z., Graybuck, L.T., Smith, K.A., Nguyen, T.N., Bertagnolli, D., Goldy, J., Garren, E., Economo, M.N., Viswanathan, S., et al. (2018). Shared and distinct transcriptomic cell types across neocortical areas. Nature *563*, 72–78. https://doi.org/10.1038/s41586-018-0654-5.

75. Pouchelon, G., Dwivedi, D., Bollmann, Y., Agba, C.K., Xu, Q., Mirow, A.M.C., Kim, S., Qiu, Y., Sevier, E., Ritola, K.D., et al. (2021). The organization and development of cortical interneuron presynaptic circuits are area specific. Cell Rep. *37*, 109993. https://doi.org/10.1016/j.celrep.2021.109993.

76. Urban-Ciecko, J., and Barth, A.L. (2016). Somatostatin-expressing neurons in cortical networks. Nat. Rev. Neurosci. *17*, 401–409. https://doi.org/10.1038/nrn.2016.53.

77. Bounds, H.A., Sadahiro, M., Hendricks, W.D., Gajowa, M., Gopakumar, K., Quintana, D., Tasic, B., Daigle, T.L., Zeng, H., Oldenburg, I.A., et al. (2023). All-optical recreation of naturalistic neural activity with a multifunctional transgenic reporter mouse. Cell Rep. *42*, 112909. https://doi.org/10.1016/j.celrep.2023.112909.

78. Pachitariu, M., Stringer, C., Dipoppa, M., Schröder, S., Rossi, L.F., Dalgleish, H., Carandini, M., and Harris, K.D. (2017). Suite2p: beyond 10,000 neurons with standard two-photon microscopy. Preprint at bioRxiv. https://doi.org/10.1101/061507.

79. Veit, J., Handy, G., Mossing, D.P., Doiron, B., and Adesnik, H. (2023). Cortical VIP neurons locally control the gain but globally control the coherence of gamma band rhythms. Neuron *111*, 405–417.e5. https://doi.org/10.1016/j.neuron.2022.10.036.

80. Margrie, T.W., Brecht, M., and Sakmann, B. (2002). In vivo, low-resistance, whole-cell recordings from neurons in the anaesthetized and awake mammalian brain. Pflugers Arch. *444*, 491–498. https://doi.org/10.1007/s00424-002-0831-z.

81. Brainard, D.H. (1997). The Psychophysics Toolbox. Spat. Vis. *10*, 433–436. https://doi.org/10.1163/156856897X00357.

82. Pégard, N.C., Mardinly, A.R., Oldenburg, I.A., Sridharan, S., Waller, L., and Adesnik, H. (2017). Three-dimensional scanless holographic optogenetics with temporal focusing (3D-SHOT). Nat. Commun. *8*, 1228. https://doi.org/10.1038/s41467-017-01031-3.

83. Mardinly, A.R., Oldenburg, I.A., Pégard, N.C., Sridharan, S., Lyall, E.H., Chesnov, K., Brohawn, S.G., Waller, L., and Adesnik, H. (2018). Precise multimodal optical control of neural ensemble activity. Nat. Neurosci. *21*, 881–893. https://doi.org/10.1038/s41593-018-0139-8.

84. Hill, D.N., Mehta, S.B., and Kleinfeld, D. (2011). Quality metrics to accompany spike sorting of extracellular signals. J. Neurosci. *31*, 8699–8705. https://doi.org/10.1523/JNEUROSCI.0971-11.2011.

85. Friedrich, J., Zhou, P., and Paninski, L. (2017). Fast online deconvolution of calcium imaging data. PLoS Comput. Biol. *13*, e1005423. https://doi.org/10.1371/journal.pcbi.1005423.

86. Lyall, E.H., Mossing, D.P., Pluta, S.R., Chu, Y.W., Dudai, A., and Adesnik, H. (2021). Synthesis of a comprehensive population code for contextual features in the awake sensory cortex. eLife *10*, e62687. https://doi.org/10.7554/eLife.62687.

Please cite this article in press as: Hendricks et al., Feature-tuned synaptic inputs to somatostatin interneurons drive context-dependent processing, Neuron (2025), https://doi.org/10.1016/j.neuron.2025.12.021

STAR★METHODS

KEY RESOURCES TABLE

REAGENT or RESOURCE	SOURCE	IDENTIFIER
Bacterial and virus strains		
PhP.eB-TRE-st-ChroME-P2A-H2B-mRuby3	Bounds et al.[77]	N/A
AAV-hSyn-DIO-eNpHR3.0-YFP	Addgene	26972-AAV1
AAV9-CAG-DIO-eNpHR3.0-mRuby3	UPenn Viral Vector Core	N/A
AAV9-hSyn-GCaMP6s	UPenn Viral Vector Core	N/A
AAV-hSyn-DIO-GCaMP6f-p2A-mTagBFP2	This paper	N/A
Deposited data		
Original Data	This paper	Zenodo: 10.5281/zenodo.17527499
Experimental models: Organisms/strains		
Mouse: tetO-GCaMP6s: B6;DBA-Tg(tetO-GCaMP6s)2Niell/J	Jackson Laboratory	RRID: IMSR_JAX: 024742
Mouse: Camk2a-tTa: B6;CBA-Tg(Camk2a-tTA)1Mmay/J	Jackson Laboratory	RRID: IMSR_JAX: 003010
Mouse: Rosa-LSL-tdTomato: B6.Cg-*Gt(ROSA)26Sor*$^{tm9(CAG\text{-}tdTomato)Hze}$/J	Jackson Laboratory	RRID: IMSR_JAX:007909
Mouse: Ai162 (TIT2L-GC6s-ICL-tTA2): B6.Cg-*Igs7*$^{tm162.1(tetO\text{-}GCaMP6s,CAG\text{-}tTA2)Hze}$/J	Jackson Laboratory	RRID: IMSR_JAX:031562
Mouse: Sst-IRES-Cre: Sst$^{tm2.1(cre)Zjh}$/J	Jackson Laboratory	RRID: IMSR_JAX:013044
Mouse: Vip-IRES-Cre: Vip$^{tm1(cre)Zjh}$/J	Jackson Laboratory	RRID: IMSR_JAX:010908
Mouse: Sst-IRES-Flp: B6J.Cg-Sst$^{tm3.1(flpo)Zjh}$/AreckJ	Jackson Laboratory	RRID: IMSR_JAX:031629
Software and algorithms		
MATLAB	MathWorks	RRID: SCR_001622
Python	Python Software Foundation	RRID: SCR_008394
Suite2p	Pachitariu et al.[78]	RRID: SCR_016434
ScanImage	Vidrio Inc.	RRID: SCR_014307
UltraMega Sort	https://neurophysics.ucsd.edu/software.php	RRID:SCR_015857
MClust	https://redishlab.umn.edu/mclust	N/A
Psychophysics Toolbox	http://psychtoolbox.org/	RRID:SCR_002881
Original code for analysis	This paper	Zenodo: 10.5281/zenodo.17527499
Other		
Spatial Light Modulator	Meadowlark	HSPDM-1K
Coherent Monaco 2p stimulation laser	Coherent	https://www.coherent.com/lasers/ultrashort-pulse/monaco

EXPERIMENTAL MODEL AND STUDY PARTICIPANT DETAILS

All experiments were approved by the University of California, Berkeley Animal Care and Use Committee. All mouse strains were purchased from Jackson labs and maintained on a C57BL/6J background. Strains used in experiments are: Sst-IRES-Cre (RRID:IMSR_JAX:013044), Vip-IRES-Cre (RRID:IMSR_JAX:010908), VIP-IRES-Cre; SST-IRES-Flp (RRID:IMSR_JAX:031629), Camk2a-tTa (RRID:IMSR_JAX:007004), tetO-GCaMP6s (RRID:IMSR_JAX:024742), Rosa-LSL-tdTomato (RRID:IMSR_JAX:007909), and Ai162 (TIT2L-GC6s-ICL-tTA2) (RRID:IMSR_JAX:031562). Mice were heterozygous for all transgenes. Experiments were performed on equal numbers of adult male and female mice. Mice were housed in cohorts of five or fewer under a reverse light:dark cycle of 12 h. Experiments were performed during the dark phase.

Please cite this article in press as: Hendricks et al., Feature-tuned synaptic inputs to somatostatin interneurons drive context-dependent processing, Neuron (2025), https://doi.org/10.1016/j.neuron.2025.12.021

METHOD DETAILS

Viral injections

SST- and VIP-IRES-Cre mice used for electrophysiology were injected neonatally (P3-P5) with AAV-hSyn-DIO-eNpHR3.0-YFP. For VIP silencing experiments, VIP-IRES-Cre; SST-IRES-Flp mice were injected neonatally with AAV9-CAG-DIO-eNpHR3.0-mRuby3, as previously described[44,79] and then as adults with AAV9-hSyn-GCaMP6s (UPenn Vector Core) immediately prior to cranial window placement.[44] For 2-photon holographic optogenetic experiments, SST-Cre; CaMK2a-tTA;tetO-GCaMP6s mice were injected with a cocktail of AAV-TRE-ChroME2s-H2B-mRuby3 and AAV-hSyn-DIO-GCaMP6f-p2A-mTagBFP2.[3] In brief, for adult viral injections, mice 6 weeks or older were anesthetized with 2% isoflurane, given 2 mg/kg of dexamethasone to control cerebral edema and 0.5 mg/kg of buprenorphine as perioperative analgesia, and place in a stereotaxic instrument for head-post implantation, viral injections, craniotomy, and window placement. Body temperature was maintained at 37°C. A small incision was made to remove the scalp and retract the fascia, and 2-3 burr holes (minimum 1 mm apart) were made with a dremel over left V1 (2.7 mm lateral, 1 mm anterior, of lambda). Virus was slowly injected (300 nL, 50 nL/min; Micro4, World Precision Instruments) through each burr hole via a beveled glass pipet (Drummond Scientific). Headplating and cranial windowing were performed immediately following viral injections. The skull was lightly scored with a drill bit and vetbond applied to improve adhesion of the dental cement and headplate. A 3.5 mm diameter opening in the skull was made with a biopsy punch and a cranial window consisting of two stacked 3 mm diameter coverslips and one 5 mm diameter coverslip on top was secured into place with dental cement (Metabond). Finally, a custom titanium headplate was cemented into place. Mice were given postoperative analgesics (0.5 mg/kg buprenorphine and 5 mg/kg meloxicam) and monitored during recovery.

Electrophysiology

In vivo *whole-cell patch clamp recording in V1*

In vivo awake whole-cell voltage clamp experiments from V1 L2/3 pyramidal cells (Figure 1) in mice were prepared as previously described,[37] following several days habituation to head restraint on a free spinning running wheel. On the day of recording, mice were briefly anesthetized with 2% isoflurane, the skull over the primary visual cortex was thinned, and a small (<300 μm) craniotomy was performed with a 27 gauge needle for electrode access. The dura was not removed. Mice were then fixed on the recording set up and allowed to recover for 10-15 min after which they ran freely on the circular treadmill. Patch electrodes (4-5 MΩ) were inserted perpendicularly to the cortex and advanced into L2/3 (<350 μm after first contact with the pia). Cells were targeted with the standard "blind" technique.[37,80] Pipettes were filled with a cesium based intracellular solution also containing QX-314 and TEA (Sigma-Aldrich) to block active conductances. Excitatory currents were measured at a holding potential of -70 mV, while inhibitory currents were measured at excitatory reversal (∼+10 mV without correction for the junction potential). Access resistance ranges from ∼20-35 MΩ and was partially compensated for via the Axopatch 200B (Molecular Devices) amplifier. After establishing whole-cell configuration at -70 mV holding potential, the visual receptive field (RF) was mapped by presenting a drifting grating stimulus (12 visual degrees) on a gamma corrected 23-inch LCD display (Eizo FORIS FS2333) positioned 10 cm from the contralateral eye, and manually moving the stimulus to the location and rotating to the preferred orientation that evoked the maximum excitatory postsynaptic current. Gratings were presented at the neuron's preferred visual stimulus. Visual stimuli were generated with the Psychophysics Toolbox.[81]

Extracellular multi-unit electrode recording in V1

For extracellular multi-unit electrode recordings (Figures 1 and 2), mice were prepared similarly as above. Rather than a patch electrode, one or two 16-channel linear electrodes with 25 micron spacing (NeuroNexus, A1x16-5mm-25-177-A16) were guided into the brain using micromanipulators (Sensapex) and a stereomicroscope (Leica) up to the depth of Layer 4 (450 μm). Electrical activity was amplified and digitized at 30 kHz (Spike Gadgets) and stored on a computer hard drive. The cortical depth of each electrical contact was determined by zeroing the bottom contact to the surface of the brain. Electrodes were inserted close to perpendicular to the brain's surface for single electrode recordings and ∼25 degrees from vertical for the two electrode experiments. After each recording a laminar probe coated with the lipophilic dye DiI was used to mark each electrode track to quantitatively assess insertion angle and depth with post hoc histologic reconstructions. The laminar depth of recorded units was corrected for the insertion angle and the local curvature of the neocortex.

Visual stimuli were generated with the Psychophysics Toolbox on an Apple Mac Mini and were presented on a gamma corrected 23-inch LCD display with a 60-Hz refresh rate (Eizo FORIS FS2333). At the beginning of each recording session the receptive fields of MUA recorded at each cortical location were mapped with sparse noise to be able to precisely position the grating stimuli. The stimulus was centered on a location where a small grating, movable by hand, elicited a clear response. Sparse noise consisted of black and white squares (2 visual degrees, 80 ms) on a 20° x 20° grid (in visual degrees) flashed onto a gray background of intermediate luminance. To improve receptive field estimation the same stimulus grid was offset by 1 degree and the resulting maps were averaged. MUA average receptive fields were calculated by reverse correlation. MUA activity was immediately analyzed offline, and the grating stimuli were then centered on the peak of the resulting population receptive field.

The center-surround stimulus consisted of full contrast drifting square-wave gratings at 0.04 cycles per degree and 2 cycles per second presented for 2 s with at least 1 s inter stimulus interval. The center grating was presented at eight (0°- 315° in steps of 45° - SOM-Cre population) or four (0° - 270° in steps of 90° - VIP-Cre population) different orientations, with a circular

aperture of 8-20° visual degrees diameter, centered on the MUA receptive field, which was surrounded by a 60 degree grating with either 0° or 90° offset (SST-Cre population) or one of seven different relative orientations (0-90° in steps of 15°, VIP-Cre population). We also presented the center grating without surrounding grating (center-only condition).

Optogenetic stimulation for extracellular multi-unit electrode recording in V1

For optogenetic stimulation of eNpHR3.0 *in vivo* (Figure 2) we use red light (center wavelength: 625 nm) from the end of a 1-mm diameter multimode optical fiber coupled to a fiber coupled LED (0.39 NA, Thorlabs) controlled by digital outputs (NI PCIe-6353). The fiber was placed as close to the craniotomy as possible (<3 mm). The illumination area was set to illuminate a wide area including all of V1. Light levels were tested in increasing intensities at the beginning of the experiment and were kept at the lowest possible level that still evoked observable change in ongoing activity for the remainder of the recording. Light power at the tip was ~4-8 mW. The red LED was switched on for 1 s starting 0.5 s after start of the visual stimulus in 50% of the trials. The period of light was chosen to influence the stable steady-state of the response to the grating, and all analysis was performed during this time window.

In vivo *targeted two-photon patch-clamp recording from V1 SST neurons*

In vivo two-photon targeted whole-cell voltage-clamp experiments from SST neurons (Figure 3) were performed in SST-Cre mice crossed with Rosa-LSL-tdTomato (SST-Cre;Ai9). Preparatory surgery of implantation of a head post with an integrated recording chamber and a 3 mm craniotomy were performed under 2% isoflurane anesthesia, sedation under chlorprothixene (5 mg/kg; intraperitoneal; Sigma-Aldrich), and cerebral edema reduction with dexamethasone (2 mg/kg; subcutaneous). The dura was removed using fine forceps. The craniotomy was left open but covered and protected with 0.9% low-melting point agarose and hydrated with artificial cerebrospinal fluid. Recordings were then performed under light anesthesia with 0.25-0.5% isoflurane. Mouse body temperature was maintained with a feedback-controlled heating pad. Under two photon visual guidance, a patch electrode (5-6 MΩ) containing cesium-based intracellular solution (containing QX-314 and TEA; Sigma-Aldrich) mixed with AlexaFluor 488 (50 μM; Thermo Fisher Scientific) was directed to the cell along an oblique angle of 24°. Continuous positive pressure was applied to the patch electrode during guidance through brain tissue to ensure visibility and clearance of the electrode tip. Contrasts in fluorescence created by background fluorescence of tdTomato and AlexaFluor 488 were used to avoid blood vessels and identify the soma of non-SST neurons. Sealing attempts were only made on somata with tdTomato expression. Access resistance ranges from ~20-35 MΩ and was partially compensated for via the Multiclamp 700B amplifier (Molecular Devices).

After establishing whole-cell configuration at -70 mV holding potential, the RF of the SST neuron was mapped by presenting a drifting grating stimulus set to the average peak of PC size tuning (12 visual degrees), on a Retina iPad LCD display (Adafruit Industries) positioned 10 cm from the contralateral eye, and manually moving the stimulus to the location and rotated to the base orientation (0°) that evoked the maximum excitatory postsynaptic current. Finally, visual evoked excitatory currents in the RF-centered SST neurons were measured in response to different visual stimulus types (“center”, “iso”, “cross”, “aperture”) across 2 orientations, 0° and orthogonal (90°). Visual stimulus center was defined as the stimulus space occupying the central 12 visual degrees, and the surround, present in “iso”, “cross”, and “aperture” was defined as the stimulus space beyond center up to 60 visual degrees. All visual stimuli were generated and presented at 1 Hz, 0.08 cycles per degree, 100% contrast using PsychtoolBox (v3.0). Similar to whole cell recordings from pyramidal cells (see above), responses are from the neuron’s preferred orientation.

One-photon optogenetics

Calcium imaging and one photon optogenetics were performed as previously described.[44] Briefly, mice were headfixed and allowed to run freely on a rotating circular treadmill under a 16x magnification objective (Nikon) and two-photon resonant scanning microscope (Neurolabware). One-photon illumination (617 nm LED, Thorlabs) for optogenetic silencing was filtered by a 613/22 nm single-bandpass filter (Semrock) and delivered through the objective at 6 mW. The PMT was protected by a shortpass filter and any remaining artifacts were subtracted in post-processing. Visual stimuli were presented using Psychtoolbox 3[81] on a LCD monitor placed 13-15 cm from the eye. Receptive fields were mapped using 10° drifting grating patches (0.08 cycles per degree, 1 Hz temporal frequency) that rotated in direction 360° over the course of 1.5 seconds. Patches were randomly interleaved within a 40° x 40° grid at 5° intervals.

Two-photon holographic optogenetics

Calcium imaging and two photon holographic optogenetics were performed similarly as previously described,[3,77] on a microscope (Sutter MOM, Sutter Instruments) adapted to be capable of simultaneous 3D imaging (resonant-galvo scanning: 3 z-planes, 30 Hz frame rate, 6.36 Hz volume rate) and 3D photostimulation (3D-SHOT).[3,77,82,83] Images were collected using ScanImage 2019 (MBF Biosciences, formerly Vidrio Technologies) with a 20X (1.0 NA) magnification water-immersion objective (Olympus). A dual band-pass dichroic mirror (Chroma, 59003m) was placed prior to the PMTs to direct blue and red light into the same PMT, avoiding GCaMP fluorescence contamination when imaging BFP cells at 830 nm, and thereby enhancing our ability to accurately detect BFP+ neurons. A swapable blue or red single band-pass filter was then used when collecting BFP or mRuby images, respectively. An electrically-tunable lens (Optotune) was placed in the imaging path immediately prior to the resonance-galvo mirrors for fast-z scanning. Imaging laser (Chameleon Ultra II, Coherent) power was restricted to <75 mW at 920 nm to minimize scanning induced crosstalk. All calcium imaging experiments were performed in L2/3 of V1. For experiments with holographic stimulation, custom MATLAB control software was used to control holographic stimulation and synchronize image acquisition.

Please cite this article in press as: Hendricks et al., Feature-tuned synaptic inputs to somatostatin interneurons drive context-dependent processing, Neuron (2025), https://doi.org/10.1016/j.neuron.2025.12.021

Holographic optogenetic stimulation was performed using a Monaco 40W laser (Coherent) directed into our custom-built 3D-SHOT optical path and temporally focused using a blazed diffraction grating (Newport Corporation). The beam was directed through a rotating diffuser to randomize the phase and expand the beam onto the spatial light modulator (SLM) (Meadowlark, HSPDM-1K). Phase masks were calculated using a weighted Gerchberg-Saxton algorithm and displayed on the SLM to generate temporally focused spots in 3D. Imaging and photostimulation paths were merged prior to the tube lens with a polarizing beamsplitter (Thorlabs). Photostimulation was synchronized to the scan phase of the resonance mirror and gated with an Arduino Mega to limit stimulation artifacts to the very edge of the imaging FOV. Tiffs were cropped post hoc to remove any remaining contamination. Imaging and photostimulation paths were first manually co-aligned then digitally calibrated[3] to achieve precise targeting and ensure an even distribution of power throughout the FOV. The calibration was verified prior to every experiment by burning holes in a thin fluorescent slide. Digital offsets were applied to the calibration to account for minor drifts (<5 μm) in co-alignment. Larger misalignments triggered a full recalibration. Slow drifts of the FOV over the course of the experiment were manually corrected, aided by the location of blood vessels and other landmarks.

Visual stimuli were presented on a 2,048 x 1536 Retina iPad LCD display (Adafruit Industries) placed 10 cm from the mouse. The display was synchronized with the galvos such that the backlight was only illuminated during the X- (resonant) galvo turnaround time to prevent light from the monitor contaminating the 2p imaging. Drifting gratings (50 visual degrees, 1 Hz, 0.08 cycles per degree, 100% contrast) of multiple directions (every 30°, between 0-330°) were shown a minimum of 10 trials for each orientation and used to determine orientation tuning. Receptive fields were mapped similarly to two-photon calcium imaging experiments without holographic optogenetics (see above).

All visual stimuli were created and presented using PsychtoolBox v3.0.[81] Tuning curves were calculated during the experiment, aided by live2p (https://github.com/willyh101/live2p), a custom implementation of CaImAn OnACID (v1.8.8) to perform rigid motion correction and seeded source extraction. Preferred orientation was determined as the orientation corresponding to the maximum mean response to drifting gratings. Visually responsive cells with a high orientation selectivity (>0.5, where OSI = ($R_{preferred}$ -$R_{orthogonal}$) - ($R_{preferred}$ + $R_{orthogonal}$) and R is the mean ΔF/F response) were selected for holographic stimulation. Due to experimental time constraints, a maximum of 10 PCs were targeted during an experiment, chosen at random from the cells after applying the aforementioned exclusion criteria.

QUANTIFICATION AND STATISTICAL ANALYSIS

Non-parametric statistical tests were performed, unless indicated otherwise. Individual field of views (FOVs) may come from the same mouse but from a different area within V1 or z-plane and therefore consist of different neurons. No statistical test was performed to predetermine sample sizes. Targeted cells passing selecting criteria were randomly selected as targeted neurons and blind to the experimenter during data collection. Batch analysis scripts were performed post hoc across experimental conditions, effectively blinding the experimenter during data analysis. In instances where plot axes are clipped to aid in visualization, statistics were performed on the unclipped and complete dataset. Statistical analysis was performed in Python. Details on statistical tests, n, and calculation of center and dispersion are specified either in the text or figure legends.

Analysis of spiking data

Spiking activity was extracted by filtering the raw signal between 800 and 7000 Hz. Spike detection was performed using the UltraMega Sort package.[84] Detected spike waveforms were sorted using the MClust package (https://redishlab.umn.edu/mclust). Waveforms were first clustered automatically using KlustaKwik and then manually corrected to meet criteria for further analysis. With the exception of a few burst firing units, included units had no more than 1.5% of their individual waveforms violating a refractory period of 2 ms. Individual units were classified as either fast-spiking or regular spiking using a k-means cluster analysis of spike waveform components. Since the best separation criterion was the trough-to-peak latency of the large negative going deflection and clustering is non-deterministic, we defined all units with latencies shorter than 0.36 ms as fast spiking and all units with latencies larger than 0.38 ms as regular spiking. Cells with intermediate latencies were excluded from further analysis. Firing rates were computed from counting spikes in a 1 s window starting 500 ms after the onset of the visual stimulus, which coincided with the onset of the LED during optogenetic suppression trials. Contextual modulation index (CMI) was calculated as CMI = (R_{cross} - R_{iso}) / (R_{cross} + R_{iso}), where R is the mean response during visual stimulation, without respect to preferred orientation. Responses are presented as the mean firing rates averaged across all orientations.

Two-photon calcium imaging analysis

Raw image files were motion corrected and ROIs were extracted using suite2p.[78] ROI selection was manually curated in suite2p based on morphology and fluorescence statistics. Neuropil for each ROI (or putative "cell") was multiplied by a correction coefficient (0.7) and subtracted from the raw fluorescence. Cellwise fluorescence was minimum subtracted, and ΔF/F was calculated as: ΔF/F = (F-F_0)/F_0, where F is the neuropil-subtracted, raw fluorescence signal, and F_0 is the baseline fluorescence, defined as the 10th percentile of fluorescence within a rolling 1-min window, applied continuously across the time series, for each cell. For a subset of experiments (Figures 2 and S2–S4), calcium traces were deconvolved using OASIS with a L1 sparsity penalty[44,85] and reported as discretized event rates. Importantly, "event rate" should not be equated with "spike rate", as the event rate reported here is unlikely

Please cite this article in press as: Hendricks et al., Feature-tuned synaptic inputs to somatostatin interneurons drive context-dependent processing, Neuron (2025), https://doi.org/10.1016/j.neuron.2025.12.021

to be a purely linear transform from calcium responses, in part due to known non-linearities in the spike to GCaMP signal transformation.[86]

Retinotopic locations for each cell were estimated by calculating the mean responses to each grid location and then fit with a 2D gaussian. Cells were then classified as "aligned" if they were within 10° of the stimulus center in retinotopic space. Tuning curves were generated by calculating the mean response to each orientation. Preferred orientation was determined as the orientation corresponding to the maximum mean response of the tuning curve. Orientation selectivity index (OSI) was calculated post hoc using a vector sum approach, $OSI = sqrt(\sum_i R_i cos(2\theta_i)^2 + \sum_i R_i sin(2\theta_i)^2) / \sum_i R_i$, where R_i are the responses to each orientation, θ_i in radians. CMI was calculated similarly to the analysis of spiking data (see STAR Methods above). Responses to center, iso, and cross visual stimuli are based on the mean visual response, without respect to preferred orientation.

Two-photon holographic optogenetics analysis

Putative SST interneurons were manually identified from a mean image collected at 830 nm. For post hoc analysis, holographic targets and BFP-positive SST cells were matched to suite2p extracted cells by the source minimizing the Euclidean distance between centroids. Offline analysis of visual responses was performed similarly to two-photon calcium imaging analysis (see above). Cells were considered visually responsive if they had a significantly different response ($p < 0.05$, ANOVA) to visual stimuli. Tuning curves for each cell were constructed by collecting the average mean ΔF/F response during visual stimulation across a minimum of 10 trials. Preferred orientation and OSI were calculated as described above. Only cells that were determined to be visually responsive and orientation-tuned (OSI > 0.33) were considered in subsequent analysis. Targeted cells and cells located closer than 15 μm radially from a targeted cell on any z-plane were also excluded from further analysis, based on existing calibrations and characterization of our microscope.[3] Tuning curves and preferred orientation of SSTs were computed similarly to PCs, as described above.

Neuron, Volume *114*

Supplemental information

Feature-tuned synaptic inputs to somatostatin interneurons drive context-dependent processing

William D. Hendricks, Masato Sadahiro, Dan Mossing, Julia Veit, and Hillel Adesnik

Supplemental Figures

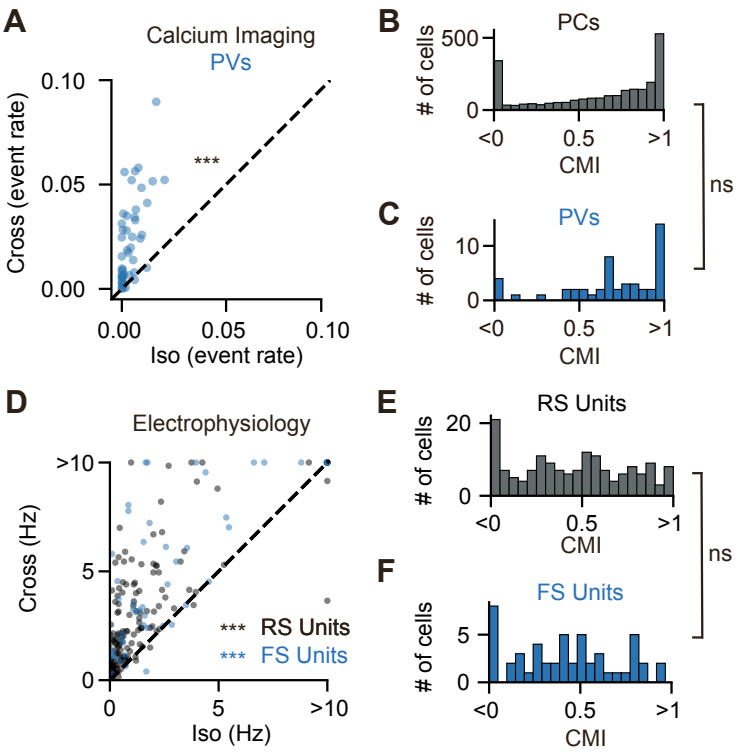

Figure S1: Orientation-tuned surround suppression in both PCs and PVs, and RS and FS units, related to Figure 2.
A: Scatter plot of deconvolved calcium responses (event rate) to cross and iso stimuli taken from PV cells (n=49 cells, $p<10^{-5}$, Wilcoxon signed-rank test).
B: Distribution of CMI in PCs (n=2,329 cells) taken from *in vivo* calcium recordings.
C: Similar to **B**, except for PVs (n=49 cells). p=0.168, Mann-Whitney U-test
D: Scatter plot of cross and iso responses from extracellular electrode recordings to cross and iso stimuli for both RS (black, n=158 units, $p<10^{-5}$, Wilcoxon signed-rank test) and FS units (blue, n=51 units, $p<10^{-5}$, Wilcoxon signed-rank test).
E: Distribution of CMI in RS units (n=158 units).
F: Similar to **E**, except for FS units (n=51 units). p = 0.430, Mann-Whitney U-test. ***p<0.001; ns, not significant

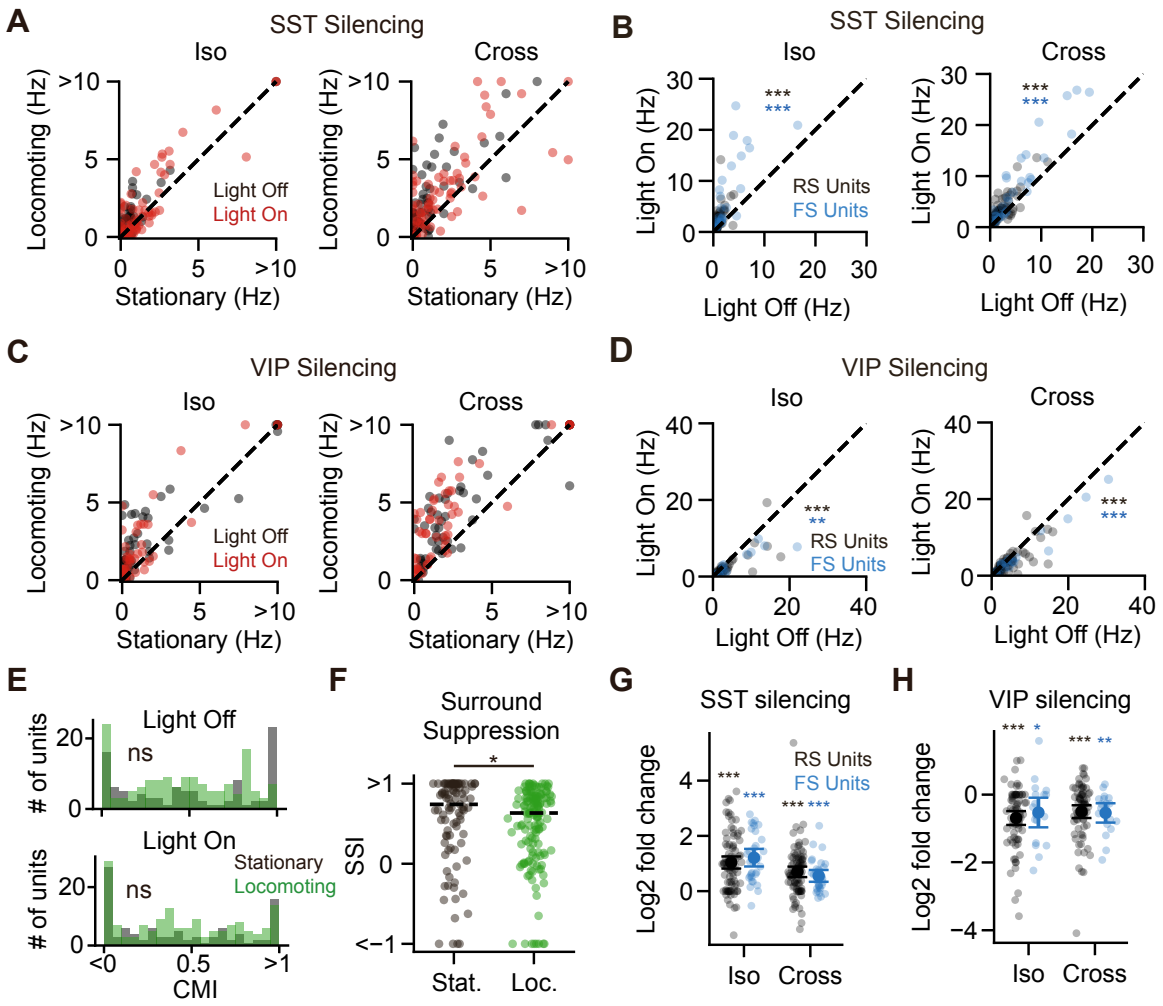

Figure S2: Effects of SST and VIP silencing on putative PC and PV firing rates, related to Figure 2.
A: Scatter plots comparing RS unit firing rates during SST silencing during iso (left) and cross (right) visual stimuli during locomoting and stationary states. Black points represent responses during control trials (light off) and red points represent firing rates during SST silencing (light on).
B: Scatter plot depicting the effect of SST silencing on RS (black dots) and FS unit (blue dots) firing rates in both the iso (left, n=87 RS units, $p<10^{-5}$, n=32 FS units, $p<10^{-5}$; Wilcoxon signed-rank tests) and cross (right, n=87 RS units, $p<10^{-5}$, n=32 FS units, $p<10^{-5}$, Wilcoxon signed-rank tests) conditions.
C: Similar to **A**, except for RS units during VIP silencing.
D: Similar to **B**, except depicting the effect of VIP silencing on RS and FS unit firing rates in both the iso (left, n=73 RS units, $p<10^{-5}$, n=19 FS units, p=0.0080, Wilcoxon signed-rank tests) and cross (right, n=73 RS units, $p<10^{-5}$, n=19 units FS units, p=0.0008, Wilcoxon signed-rank tests) conditions.
E: RS-unit CMI during stationary (black) and locomoting (green) states for light off (top) and light on (bottom) conditions (CMI, light off: stationary, n=98 RS-units; locomoting, n=150 RS units, p=0.393, Mann-Whitney U-test; CMI, light on: stationary, n=101 RS-units; locomoting, n=154 RS-units, p=0.350, Mann-Whitney U-test).
F: Surround suppression to iso gratings during stationary (left, black dots) and locomoting (right, green dots) trials (SSI: Surround suppression index, stationary: n=96 RS units, locomoting: n=146 RS units, p=0.015, Mann-Whitney U-test). Dashed line represents the median of the distribution.
G: Quantification of log2 fold change in RS (black dots) and FS unit (blue dots) firing rates in response to SST silencing to both iso (n=87 RS units, $p<10^{-5}$, n=32 FS units, p< $p<10^{-5}$, one-sample Wilcoxon signed-rank tests) and cross (n=87 RS units, $p<10^{-5}$, n=32 FS units, $p<10^{-5}$, one-sample Wilcoxon signed-rank tests) conditions.
H: Similar to **G**, except during VIP silencing to both iso (n=73 RS units, $p<10^{-5}$, n=19 FS units, p=0.019, one-sample Wilcoxon signed-rank tests) and cross (n=73 RS units, $p<10^{-5}$, n=19 FS units, p=0.0013, one-sample Wilcoxon signed-rank tests) conditions. Data are presented as mean ± SEM unless otherwise noted. *p<0.05, **p<0.01, ***p<0.001; ns, not significant

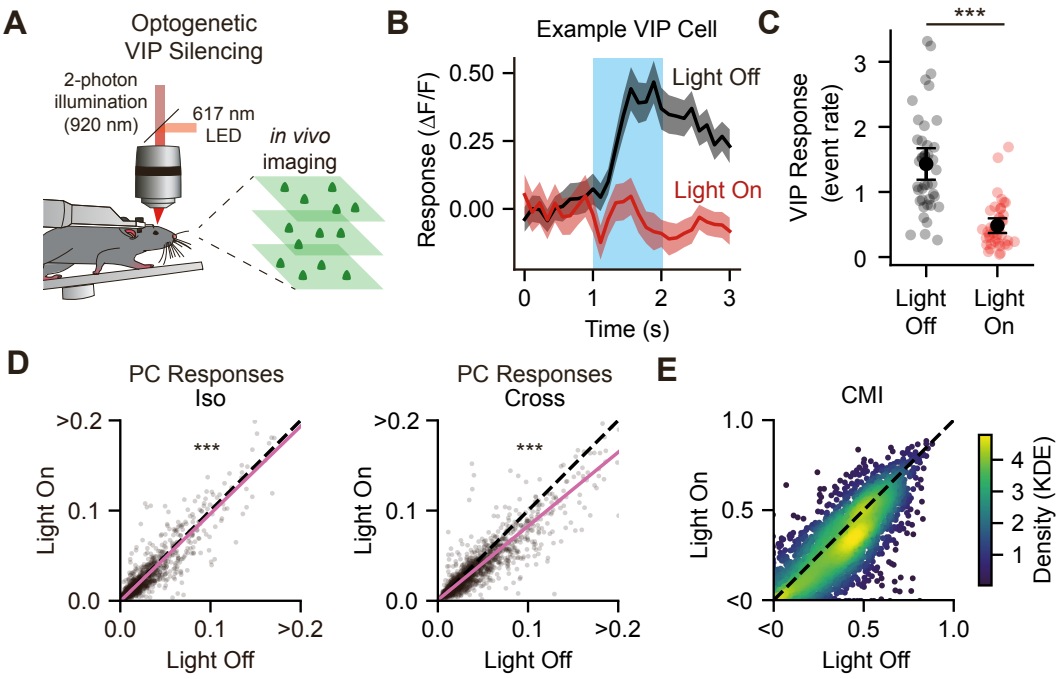

Figure S3: Optogenetic silencing of VIPs, related to Figure 2.
A: Schematic depicting approach for simultaneous *in vivo* 2-photon calcium imaging and one-photon optogenetic VIP silencing.
B: Visually evoked response (mean ΔF/F) of a representative VIP during optogenetic silencing trials ("light on", red) and control trials ("light off", black). Light blue shading depicts duration of the visual stimuli.
C: Quantification of **B** for all retinotopically aligned VIPs (n=41 cells, $p<10^{-5}$, Wilcoxon signed-rank test).
D: Scatter plot of visually evoked responses (deconvolved event rate) of PCs (n=2,408 cells) during control ("light off", x-axis) and optogenetic VIP silencing ("light on", y-axis) in response to iso (left, $p<10^{-5}$, Wilcoxon signed-rank test) and cross (right, $p<10^{-5}$, Wilcoxon signed-rank test) gratings. Pink lines depict the linear regression between light on and light off conditions, computed using the Moore-Penrose pseudoinverse. Axes have been cropped to a max event rate of 0.2 for clarity.
E: Scatter plot comparing CMI of PCs in light on (y-axis) and light off (x-axis) conditions (n=2,408 cells, $p<10^{-5}$, Wilcoxon signed-rank test). Individual points are colored by their kernel density estimate (K.D.E.) to highlight regions of higher data concentration. Data are presented as mean ± SEM unless otherwise noted. ***p<0.001

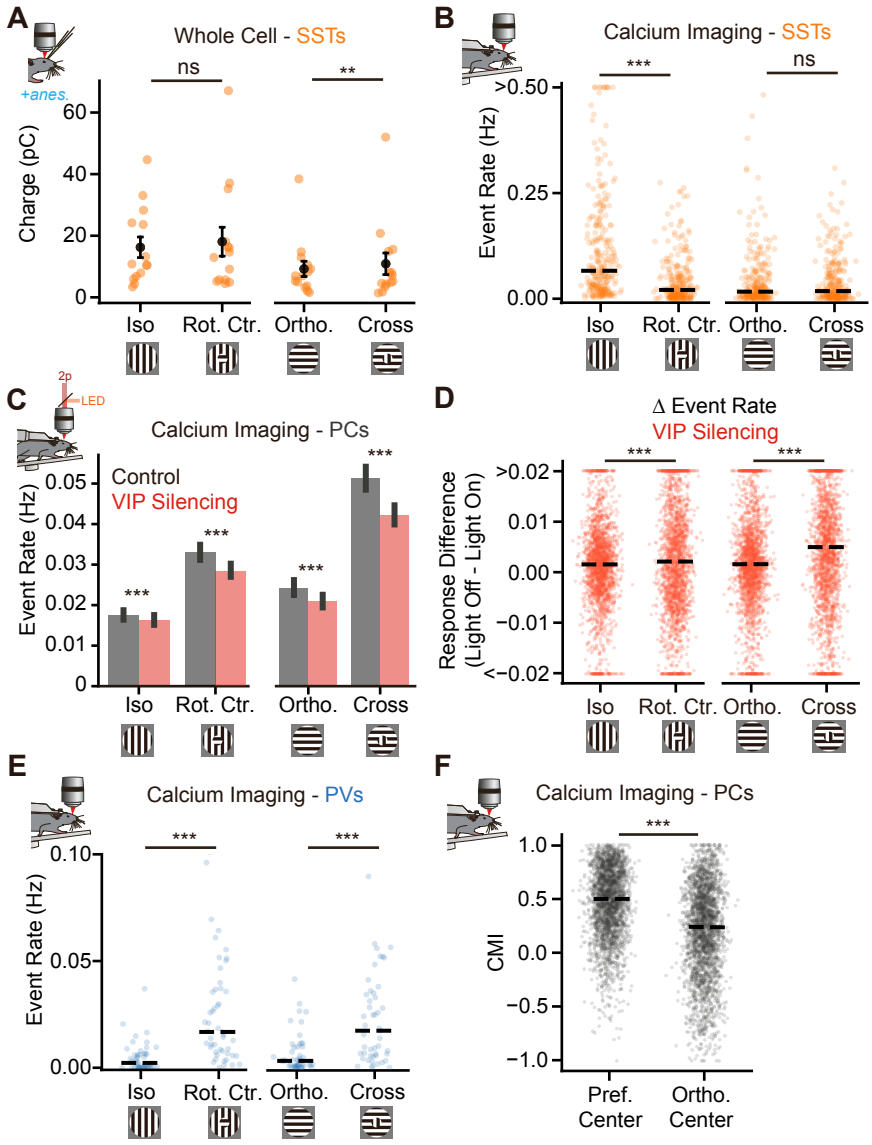

Figure S4: SST and PC responses to constant surround with rotated center stimuli, related to Figure 3.
A: Visually evoked synaptic responses to iso (preferred orientation and preferred size for SSTs), rotated center (rot. ctr.), orthogonal (ortho.), and cross stimuli (n=13 cells; iso vs. rot. ctr., p=0.827, ortho. vs. cross, p=0.00049, Wilcoxon signed-rank test). SST orientation tuning is determined by their responses to large (iso) gratings.
B: Similar to **A**, but for data collected from SSTs during calcium imaging experiments (n=271cells; iso vs. rot. ctr., $p<10^{-5}$, ortho. vs. cross, p=0.0867, Wilcoxon signed-rank test). Dashed line represents the median of the distribution.
C: Similar to **B**, but for data collected from PCs during calcium imaging experiments during control (grey) and VIP silencing (red) trials (n=2,405 cells; all conditions $p<10^{-5}$, Wilcoxon signed-rank test). Note that here, PC orientation tuning is determined by their responses to a center-only grating, not the iso grating.
D: Cellwise differences in response between light off and light on conditions from **C** for each visual stimulus condition (n=2,405 cells; iso vs. rot. ctr., $p<10^{-5}$, ortho. vs. cross, $p<10^{-5}$, Wilcoxon signed-rank test). Dashed line represents the median of the distribution.
E: Similar to **B**, but for data collected from PVs (n=49 cells, iso vs. rot. ctr., $p<10^{-5}$, ortho vs. cross, $p<10^{-5}$, Wilcoxon signed-rank test). Dashed line represents the median of the distribution. Similar to PCs, a center-only grating was used to determine PV orientation tuning.
F: Comparison of cross and iso responses in PCs (as measured by CMI) where the center stimulus was at the preferred (left) or orthogonal (right) orientation (n=2,405 cells, pref. center vs. ortho. center, $p<10^{-5}$, Wilcoxon signed-rank test). Unless otherwise noted, data are presented as mean ± SEM. **p<0.01, ***p<0.001; ns, not significant

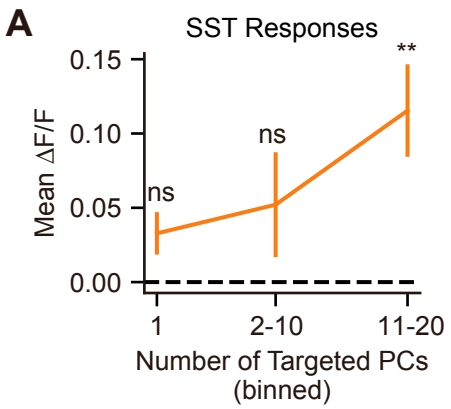

Figure S5: SST responses by PC ensemble size, related to Figure 4.
A: Mean calcium responses of SST cells while varying the number of simultaneously holographically photostimulated PCs, binned into groups of 1 (n=194 pairs, p=0.072), 2-10 (n=74 pairs, p=0.508), and 11-20 (124 pairs, p=0.004) targeted cells. A 1-sample Wilcoxon signed rank test was used to calculate p-values. Data are presented as mean ± SEM. **p<0.01; ns, not significant